



Local force calculations by an improved stress tensor discontinuity-based immersed boundary–lattice Boltzmann method

Cite as: Phys. Fluids **33**, 047104 (2021); <https://doi.org/10.1063/5.0044268>

Submitted: 15 January 2021 . Accepted: 07 March 2021 . Published Online: 05 April 2021

 Kosuke Suzuki (鈴木康祐), Kou Ishizaki (石崎攻), and  Masato Yoshino (吉野正人)

COLLECTIONS

Paper published as part of the special topic on [Special Issue on the Lattice Boltzmann Method](#)



View Online



Export Citation



CrossMark

ARTICLES YOU MAY BE INTERESTED IN

[Full-scale simulation of self-propulsion for a free-running submarine](#)

Physics of Fluids **33**, 047103 (2021); <https://doi.org/10.1063/5.0041334>

[A three-dimensional phase-field lattice Boltzmann method for incompressible two-components flows](#)

Physics of Fluids **33**, 043315 (2021); <https://doi.org/10.1063/5.0046875>

[On the lattice Boltzmann method and its application to turbulent, multiphase flows of various fluids including cryogenics: A review](#)

Physics of Fluids **33**, 041302 (2021); <https://doi.org/10.1063/5.0046938>

Physics of Fluids

SPECIAL TOPIC: Tribute to
Frank M. White on his 88th Anniversary

SUBMIT TODAY!



Local force calculations by an improved stress tensor discontinuity-based immersed boundary–lattice Boltzmann method

Cite as: Phys. Fluids **33**, 047104 (2021); doi: [10.1063/5.0044268](https://doi.org/10.1063/5.0044268)

Submitted: 15 January 2021 · Accepted: 7 March 2021 ·

Published Online: 5 April 2021



View Online



Export Citation



CrossMark

Kosuke Suzuki (鈴木康祐),^{1,a)} Kou Ishizaki (石崎政),² and Masato Yoshino (吉野正人)^{1,b)}

AFFILIATIONS

¹Institute of Engineering, Academic Assembly, Shinshu University, Nagano 380-8553, Japan

²Department of Engineering, Graduate School of Science and Technology, Shinshu University, Nagano 380-8553, Japan

Note: This paper is part of the Special Issue on the Lattice Boltzmann Method.

^{a)}Author to whom correspondence should be addressed: kosuzuki@shinshu-u.ac.jp

^{b)}Electronic mail: masato@shinshu-u.ac.jp

ABSTRACT

In the immersed boundary method, the volume force that is applied to enforce the no-slip boundary condition is equivalent to a discontinuity in the stress tensor across the boundary. In the stress tensor discontinuity-based immersed boundary–lattice Boltzmann method, which was proposed in our previous study [Suzuki and Yoshino, “A stress tensor discontinuity-based immersed boundary–lattice Boltzmann method,” *Comput. Fluids* **172**, 593–608 (2018)], the boundary is represented by Lagrangian points that are independent of the background grid, and the discontinuity in the stress tensor is calculated on these points from desired particle distribution functions that satisfy the no-slip boundary condition based on the bounce-back condition. Although this method allows computation of the force locally acting on the boundary, the local force has a spurious oscillation along the boundary. In the present study, we remedy this problem by relaxing the bounce-back condition. To confirm the improvement achieved by using the new method, we apply it to simulate typical benchmark problems involving two- and three-dimensional flows with stationary or moving boundaries. We find that the proposed approach can effectively eliminate the spurious oscillation of the local force, and the results obtained with the improved method show good agreement with other numerical and experimental results. In addition, as an application of the proposed method to local force calculation, we investigate the effect of lift enhancement due to wing–wake interaction on a two-dimensional butterfly-like flapping wing.

Published under license by AIP Publishing. <https://doi.org/10.1063/5.0044268>

NOMENCLATURE

b	number of fictitious particles
c	particle velocity
\hat{c}	dimensional characteristic speed of fictitious particles (m/s)
d	dimensionality
E	weight coefficients in the local equilibrium distribution function
f	particle distribution function
F	total force acting on the boundary
$F^{\text{not}}, F^{\text{bb}}$	PDFs that pass through the boundary without the bounce-back condition and that bounce back from the boundary with the bounce-back condition, respectively
g	volume force

$\hat{H}_0, \hat{U}_0, \hat{t}_0$	dimensional characteristic length (m), flow speed (m/s), and time (s), respectively
n	unit normal vector of the boundary
N	number of boundary Lagrangian points
p	pressure
P	local stress acting on the boundary
R	radius of the area where the preprocessing is applied
Sh	Strouhal number
t	time
T	total torque acting on the boundary
U	velocity related to the boundary
u	flow velocity
W	weighting function in the IBM
X	position related to the boundary
x	coordinates

Greek symbols

α_b	relaxation range
ΔS	small area element
Δt	time step
ΔV	small volume element
Δx	lattice spacing
ν	kinematic viscosity coefficient
ξ	thickness of the interface of the smoothed profile
ϕ	smoothed profile in the preprocessing
$\hat{\rho}_f$	dimensional fluid density (kg/m^3)
σ	stress tensor
τ	relaxation time
χ	relaxation coefficient

Superscripts

eq	local equilibrium
*	temporary value without regarding the boundary
**	corrected temporary value after preprocessing
$[\ell]$	fluid # ℓ ($\ell = 1$: external fluid, $\ell = 2$: internal fluid)

Subscripts

c	center of the body
in	inside the boundary
i	i-th fictitious particle
k	k-th boundary Lagrangian point
p	preprocessing
α, β	coordinates x, y , or z

Acronyms

IBM	immersed boundary method
IB-LBM	immersed boundary–lattice Boltzmann method
LBM	lattice Boltzmann method
PDF	particle distribution function

I. INTRODUCTION

One of the important tasks of computational fluid dynamics is efficient and accurate simulation of moving-boundary flows. Recently, the immersed boundary method (IBM), which was proposed by Peskin^{1,2} in the 1970s to simulate blood flows in the heart, has been reconsidered as an efficient method for simulating moving-boundary flows on a fixed Cartesian grid. In the IBM, the boundary is regarded as an infinitely thin shell, the regions both inside and outside the boundary are filled with an incompressible viscous fluid, and the no-slip condition on the boundary is satisfied by a volume force applied only near the boundary. The determination of the volume force is key to the IBM, and a number of variations of the IBM have been proposed, based on different ways to determine the volume force, as reviewed by Mittal and Iaccarino.³

In the case where the boundary is the surface of a solid body that does not deform, one of these variations, the direct-forcing method,⁴ has often been applied. In this method, the boundary is represented by a set of discrete points (boundary points), and the volume force on these boundary points is determined by the difference between the temporary velocity obtained without the effect of the boundary and

the desired velocity determined by the no-slip condition. The volume force is then distributed to the lattice points near the boundary points. There are a number of variations of the direct-forcing method, and these can be categorized as sharp-interface schemes or diffuse-interface schemes,⁵ depending on the arrangement of the boundary points and on the range of the lattice points to which the volume force is distributed.

In a sharp-interface scheme, the boundary points are typically set as the intersection points of the boundary with the grid lines. The volume force is extrapolated from the boundary points to the lattice points along the grid lines. The pioneering work on this type of direct-forcing method was done by Fadlun *et al.*⁶ Since a sharp-interface scheme can sharply capture the boundary, the pressure and velocity near the boundary can be computed accurately, and therefore the force locally acting on the boundary can be obtained through the stress tensor. In moving-boundary flows, however, the boundary points have to be reset at every time step, and this makes the algorithm of the sharp-interface scheme very complicated. In addition, the force acting on the boundary can suffer from spurious oscillations in time.⁷

In a diffuse-interface scheme, on the other hand, the boundary points are set as Lagrangian points that move together with a solid body, and therefore the boundary points can be defined independently of the background grid. The volume force is distributed to the lattice points using a weighting function, which was originally represented as a regularized delta function.⁸ This type of direct-forcing method was first proposed by Uhlmann.⁹ Since the algorithm for a diffuse-interface scheme depends neither on the shape of the boundary nor on whether the boundary is stationary or moving, such a scheme can be easily implemented even for complex moving-boundary flows. However, it is difficult to compute the stress tensor locally acting on the boundary using a diffuse-interface scheme, since the boundary has an effective thickness because the volume force is distributed using a weighting function.^{10,11} Although the normal probe approach,^{12,13} in which the stress tensor is calculated at the external points outside the effective thickness and then extrapolated to the boundary points, can successfully give the stress tensor locally acting on the boundary, it requires some additional procedures for interpolation and extrapolation.

Thus, both sharp-interface and diffuse-interface schemes have their respective advantages and disadvantages, and we cannot affirm that one is better than the other overall. In general, therefore, it is worthwhile attempting to remedy their defects. In the present study, we focus on one of the disadvantages of diffuse-interface schemes, namely, the difficulty in computing the stress tensor locally acting on the boundary. In our previous study,¹⁴ we proposed the stress tensor discontinuity-based immersed boundary–lattice Boltzmann method (IB-LBM) as a diffuse-interface scheme that can overcome this difficulty. In the stress tensor discontinuity-based IB-LBM, the flow field is computed using the lattice Boltzmann method (LBM), where finite-difference equations for particle distribution functions (PDFs) of a modeled gas (which is composed of identical fictitious particles whose velocities are restricted to a finite set of vectors¹⁵) are solved, and the macroscopic variables such as the pressure and velocity are calculated as moments of the PDFs. The discontinuity in the stress tensor is then calculated on the boundary points from desired PDFs that satisfy the no-slip boundary condition based on the bounce-back condition.¹⁶ The volume force is determined by the discontinuity of the stress

tensor.¹⁴ Using this method, we can compute the force locally acting on the boundary from the stress tensor on the boundary points. However, this method has suffered from a spurious oscillation of the local force, not in time but along the boundary.

This spurious oscillation of the local force along the boundary in the stress tensor discontinuity-based IB-LBM appears near the boundary points where their normal vectors on the boundary are parallel or inclined by 45° to the grid lines. A similar spurious oscillation can be observed for the interpolated bounce-back condition,¹⁷ which is a particular technique used in the LBM to satisfy the no-slip condition on curved boundaries.^{18,19} Therefore, we can consider this problem to originate from the bounce-back condition. In the present study, we identify the cause of the spurious oscillation as the fact that the set of desired PDFs given by the bounce-back condition can suddenly change along the boundary. To avoid such a sudden change, we consider a relaxation of the bounce-back condition. We show that this can effectively eliminate the spurious oscillation of the local force along the boundary in many benchmark problems. In addition, as an application of the proposed method to local force calculation, we investigate the effect of lift enhancement due to wing–wake interaction on a two-dimensional butterfly-like flapping wing.

It should be noted that the spurious oscillation of the local force along the boundary is a unique problem that has not been considered before. The first one in diffuse-interface direct-forcing IB-LBMs was proposed by Feng and Michaelides.²⁰ This method was based on the same idea as the direct-forcing method proposed by Uhlmann.⁹ Then, Niu *et al.*²¹ proposed a momentum exchange-based IB-LBM, where the volume force is determined from the amount of the momentum exchange between the desired PDFs given by the bounce-back condition and the PDFs without regard to the boundary. After that, with the aim of improving the accuracy of the no-slip condition to prevent penetration of fluid across the boundary, several IB-LBMs have been proposed such as an implicit velocity correction-based IB-LBM²² and multi-direct forcing IB-LBMs.^{5,23} These methods include the procedure to solve a large inverse matrix or to iterate interpolation and extrapolation, for determining the volume force. A trend in recent studies (e.g., Refs. 24–26) is to reduce the computational cost by avoiding these procedures while keeping the accuracy of the no-slip condition. However, all the above studies have not aimed to calculate the force locally acting on the boundary, and therefore the spurious oscillation of the local force has not been recognized as a problem. Although a similar spurious oscillation was found in a diffuse-interface IBM with a finite-volume method for the Navier–Stokes equations,²⁷ the source of the spurious oscillation was attributed to the fact that the equation for the volume force is an ill-posed integral equation of the first kind, i.e., not related to the LBM. Therefore, the issue addressed in the present study is unique and provides a new insight of the local force calculation in the framework of the diffuse-interface scheme.

The remainder of the paper is organized as follows. In Sec. II, we describe the stress tensor discontinuity-based IB-LBM with relaxation of the bounce-back condition. In Sec. III, we validate this method through benchmark problems involving two- and three-dimensional flows with stationary or moving boundaries. In Sec. IV, we apply the method to local force calculations on a two-dimensional butterfly-like flapping wing to investigate wing–wake interaction. We conclude in Sec. V.

II. STRESS TENSOR DISCONTINUITY-BASED IMMERSED BOUNDARY–LATTICE BOLTZMANN METHOD

The stress tensor discontinuity-based IB-LBM has already been described in Ref. 14, albeit without the relaxation of the bounce-back condition introduced below in Sec. II C. However, we describe it again here to help readers understand the algorithm of the method.

A. Lattice Boltzmann method

In the LBM, a gas is modeled as consisting of identical fictitious particles whose velocities are restricted to a finite set of vectors.¹⁵ A two-dimensional lattice with 9 velocity vectors (the D2Q9 model) and a three-dimensional lattice with 15 velocity vectors (the D3Q15 model) are considered in the present study. In the following, we use nondimensional variables normalized by a characteristic length \hat{H}_0 , a characteristic particle speed \hat{c} , a characteristic timescale $\hat{t}_0 = \hat{H}_0/\hat{U}_0$ (where \hat{U}_0 is a characteristic flow speed), and a fluid density $\hat{\rho}_f$, as shown in Appendix A.

The D2Q9 model has the velocity vectors $\mathbf{c}_i = (0, 0)$, $(0, \pm 1)$, $(\pm 1, 0)$, and $(\pm 1, \pm 1)$ for $i = 1, 2, \dots, 9$. The D3Q15 model has the velocity vectors $\mathbf{c}_i = (0, 0, 0)$, $(0, 0, \pm 1)$, $(0, \pm 1, 0)$, $(\pm 1, 0, 0)$, and $(\pm 1, \pm 1, \pm 1)$ for $i = 1, 2, \dots, 15$. The evolution of the PDF $f_i(\mathbf{x}, t)$ with the velocity \mathbf{c}_i at a point \mathbf{x} and time t is computed as follows:

$$f_i(\mathbf{x} + \mathbf{c}_i \Delta x, t + \Delta t) = f_i(\mathbf{x}, t) - \frac{1}{\tau} [f_i(\mathbf{x}, t) - f_i^{\text{eq}}(p(\mathbf{x}, t), \mathbf{u}(\mathbf{x}, t))], \quad (1)$$

where Δx is the lattice spacing, Δt is the time step during which the particles travel one lattice spacing, f_i^{eq} is the equilibrium PDF, and τ is the relaxation time, which is $O(1)$. Note that $\Delta t = Sh \Delta x$ where Sh is the Strouhal number defined by $Sh = \hat{H}_0/(\hat{t}_0 \hat{c}) = \hat{U}_0/\hat{c} = O(\Delta x)$, since \hat{U}_0/\hat{c} is $O(\Delta x)$ in the LBM.

The equilibrium PDF f_i^{eq} of the incompressible model²⁸ is given by

$$f_i^{\text{eq}}(p, \mathbf{u}) = E_i \left[3p + 3\mathbf{c}_i \cdot \mathbf{u} + \frac{9}{2} (\mathbf{c}_i \cdot \mathbf{u})^2 - \frac{3}{2} \mathbf{u} \cdot \mathbf{u} \right], \quad (2)$$

where $E_1 = 4/9$, $E_2 = \dots = E_5 = 1/9$, and $E_6 = \dots = E_9 = 1/36$ for the D2Q9 model, and $E_1 = 2/9$, $E_2 = \dots = E_7 = 1/9$, and $E_8 = \dots = E_{15} = 1/72$ for the D3Q15 model. The pressure $p(\mathbf{x}, t)$ and the flow velocity $\mathbf{u}(\mathbf{x}, t)$ are calculated by

$$p = \frac{1}{3} \sum_{i=1}^b f_i, \quad (3)$$

$$\mathbf{u} = \sum_{i=1}^b f_i \mathbf{c}_i, \quad (4)$$

where $b = 9$ for the D2Q9 model and $b = 15$ for the D3Q15 model. In addition, we can also calculate the stress tensor $\boldsymbol{\sigma} = \{\sigma_{\alpha\beta}\}$ ($\alpha, \beta = x, y, z$) as follows:

$$\sigma_{\alpha\beta} = -\frac{1}{2\tau} p \delta_{\alpha\beta} - \frac{\tau - \frac{1}{2}}{\tau} \left[\sum_{i=1}^b f_i (c_{i\alpha} - u_\alpha)(c_{i\beta} - u_\beta) - (3p - 1)u_\alpha u_\beta \right], \quad (5)$$

where $\delta_{\alpha\beta}$ is the Kronecker delta. The derivation of Eq. (5) is given in Ref. 14. The kinematic viscosity ν of the fluid is given by

$$\nu = \frac{1}{3} \left(\tau - \frac{1}{2} \right) \Delta x. \quad (6)$$

As described in Ref. 29, the solutions of Eqs. (1)–(4) give the pressure and the flow velocity for incompressible viscous fluid flows with relative errors $O((\Delta x)^2)$.

When an external volume force $\mathbf{g}(\mathbf{x}, t)$ is applied, the evolution equation (1) of the PDF $f_i(\mathbf{x}, t)$ can be calculated in a stepwise fashion as follows:

- (1) Evolve the PDF $f_i(\mathbf{x}, t)$ without the volume force,

$$\begin{aligned} f_i^*(\mathbf{x} + \mathbf{c}_i \Delta x, t + \Delta t) \\ = f_i(\mathbf{x}, t) - \frac{1}{\tau} [f_i(\mathbf{x}, t) - f_i^{\text{eq}}(p(\mathbf{x}, t), \mathbf{u}(\mathbf{x}, t))]. \end{aligned} \quad (7)$$

- (2) Correct the temporary PDF f_i^* by the volume force,

$$f_i(\mathbf{x}, t + \Delta t) = f_i^*(\mathbf{x}, t + \Delta t) + 3\Delta x E_i \mathbf{c}_i \cdot \mathbf{g}(\mathbf{x}, t + \Delta t). \quad (8)$$

B. Preprocessing by smoothed-profile method

To prevent penetration of fluid across the boundary, we enforce the velocity of a rigid body on the internal fluid inside the boundary as in the smoothed-profile method (SPM)^{30,31} as a preprocessing.

In the preprocessing for a circular cylinder or a sphere with center located at \mathbf{X}_c and with diameter D , we use the following smoothed profile:

$$\phi(\mathbf{x}) = s(R - |\mathbf{x} - \mathbf{X}_c|), \quad (9)$$

where \mathbf{x} is a lattice point, R is the radius of the area where the preprocessing is applied, and s is the function,

$$tpts(r) = \begin{cases} 0 & (r < -\xi/2), \\ \frac{1}{2} \left[\sin\left(\frac{\pi r}{\xi}\right) + 1 \right] & (|r| \leq \xi/2), \\ 1 & (r > \xi/2), \end{cases} \quad (10)$$

where ξ is the thickness of the interface of the profile. In this study, the parameters R and ξ are set to $R = 0.5D - 0.5\Delta x$ and $\xi = \Delta x$ so that the area where the preprocessing is applied does not interfere with the calculation of the volume force on the boundary points. According to the algorithm presented by Mino *et al.*,³² the preprocessing volume force is calculated as follows:

$$\mathbf{g}_p(\mathbf{x}, t + \Delta t) = \phi(\mathbf{x}, t + \Delta t) \frac{Sh}{\Delta t} [\mathbf{U}_{\text{in}}(\mathbf{x}, t + \Delta t) - \mathbf{u}^*(\mathbf{x}, t + \Delta t)], \quad (11)$$

where $\mathbf{U}_{\text{in}}(\mathbf{x})$ is the velocity of the body at a lattice point \mathbf{x} inside the boundary [e.g., $\mathbf{U}_{\text{in}}(\mathbf{x}) = \mathbf{0}$ for a stationary body], $\mathbf{u}^*(\mathbf{x}, t + \Delta t)$ is the temporary flow velocity calculated from Eq. (4) using the temporary PDF $f_i^*(\mathbf{x}, t + \Delta t)$, and Sh is the Strouhal number described in Sec. II A.

Finally, the temporary PDF is corrected by $\mathbf{g}_p(\mathbf{x}, t + \Delta t)$ using Eq. (8) as follows:

$$f_i^{**}(\mathbf{x}, t + \Delta t) = f_i^*(\mathbf{x}, t + \Delta t) + 3\Delta x E_i \mathbf{c}_i \cdot \mathbf{g}_p(\mathbf{x}, t + \Delta t). \quad (12)$$

C. Calculation of the volume force from the discontinuity in the stress tensor

Suppose that the temporary PDF after preprocessing, $f_i^{**}(\mathbf{x}, t + \Delta t)$, has been obtained. Let $\mathbf{X}_k(t + \Delta t)$ and $\mathbf{U}_k(t + \Delta t)$ ($k = 1, 2, \dots, N$) be the positions of the Lagrangian points of the moving boundary and the boundary velocities at these points, respectively. Denote the fluids separated by the boundary as fluids #1 and #2, and let $\mathbf{n}_k(t + \Delta t)$ be the unit normal vector of the boundary at the Lagrangian point $\mathbf{X}_k(t + \Delta t)$ pointing to fluid #1 (see Fig. 1). Note that the boundary Lagrangian points \mathbf{X}_k generally differ from the background lattice points \mathbf{x} . Then, the temporary PDF after preprocessing, $f_i^{**}(\mathbf{X}_k, t + \Delta t)$, at a boundary Lagrangian point \mathbf{X}_k is interpolated by

$$f_i^{**}(\mathbf{X}_k, t + \Delta t) = \sum_{\mathbf{x}} f_i^{**}(\mathbf{x}, t + \Delta t) W(\mathbf{x} - \mathbf{X}_k) (\Delta x)^d, \quad (13)$$

where $\sum_{\mathbf{x}}$ denotes the summation over all lattice points \mathbf{x} , d is the dimensionality, and W is the following weighting function proposed by Peskin:⁸

$$W(x, y, z) = \frac{1}{\Delta x} w\left(\frac{x}{\Delta x}\right) \frac{1}{\Delta x} w\left(\frac{y}{\Delta x}\right) \frac{1}{\Delta x} w\left(\frac{z}{\Delta x}\right), \quad (14)$$

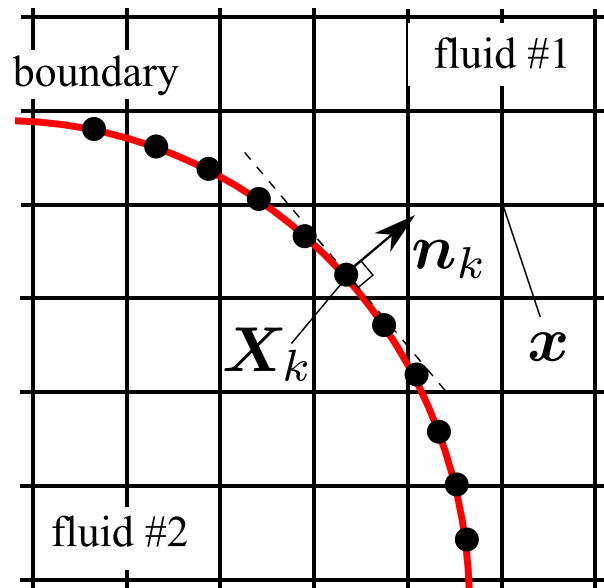


FIG. 1. Illustration of the boundary Lagrangian points \mathbf{X}_k , the unit normal vectors \mathbf{n}_k at these points, and the lattice points \mathbf{x} .

with

$$w(r) = \begin{cases} \frac{1}{8} (3 - 2|r| + \sqrt{1 + 4|r| - 4r^2}) & (|r| \leq 1), \\ \frac{1}{8} (5 - 2|r| - \sqrt{-7 + 12|r| - 4r^2}) & (1 \leq |r| \leq 2), \\ 0 & (\text{otherwise}). \end{cases} \quad (15)$$

It should be noted that Eq. (14) shows that the three-dimensional weighting function is the product of three one-dimensional weighting functions, and the two-dimensional weighting function can be obtained as the product of two one-dimensional weighting functions.

In the original method,¹⁴ the desired PDFs on the boundary are obtained using the bounce-back condition.¹⁶ However, the set of desired PDFs can suddenly change along the boundary. For example, when the tangential plane of the boundary is inclined by 45° to the horizontal grid line in two dimensions (see the left-hand side of Fig. 2), the set of desired PDFs is $\{f_2, f_3, f_6\}$. When the tangential plane is slightly changed and inclined by $45^\circ + \delta$ (see the right-hand side of Fig. 2), the set of desired PDFs is $\{f_2, f_3, f_6, f_9\}$. Therefore, the set of desired PDFs can be suddenly changed even for a slight change in the tangential plane. This causes the spurious oscillation of the local force along the boundary.

In the present study, therefore, we consider a relaxation of the bounce-back condition depending on the relationship between the normal vector \mathbf{n}_k and the particle velocity vector \mathbf{c}_i in order to avoid such a sudden change. A conceptual image of this relaxation is shown in Fig. 3. We set the buffer region between two planes, each of which is inclined by an angle α_b to the tangential plane of the boundary. In this buffer region, the PDFs that pass through the boundary and the PDFs that bounce back from the boundary are summed by weighting a relaxation coefficient. This relaxation of the bounce-back condition is the new idea in the present study.

The calculation of the desired PDFs with relaxation of the bounce-back condition proceeds as follows. The desired PDFs $f_i^{[1]}$ and $f_i^{[2]}$ that satisfy the no-slip condition on a boundary Lagrangian point \mathbf{X}_k in fluids #1 and #2, respectively, are obtained as

$$f_i^{[1]} = \begin{cases} F_i^{\text{not}} & (\mathbf{n}_k \cdot \mathbf{c}_i \leq 0), \\ (1 - \chi)F_i^{\text{not}} + \chi F_i^{\text{bb}} & (0 < \mathbf{n}_k \cdot \mathbf{c}_i \leq |\mathbf{c}_i| \sin \alpha_b), \\ F_i^{\text{bb}} & (\mathbf{n}_k \cdot \mathbf{c}_i > |\mathbf{c}_i| \sin \alpha_b), \end{cases} \quad (16)$$

and

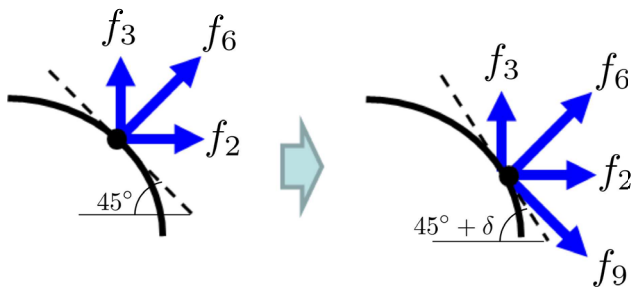


FIG. 2. Illustration of a two-dimensional example where the set of desired PDFs is suddenly changed along the boundary. Left: the tangential plane of the boundary is inclined by 45° to the horizontal grid. Right: the tangential plane is slightly changed and inclined by $45^\circ + \delta$, where $\delta > 0^\circ$. The arrows represent the directions of the desired PDFs.

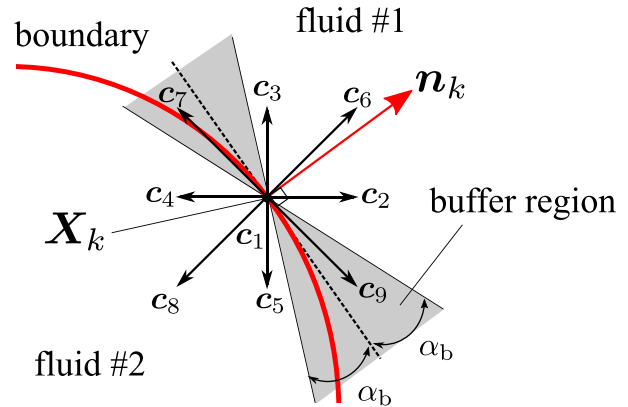


FIG. 3. Illustration of the buffer region for relaxation of the bounce-back condition. The buffer region is the region between the two planes inclined by an angle α_b from the tangential plane of the boundary.

$$f_i^{[2]} = \begin{cases} F_i^{\text{not}} & (\mathbf{n}_k \cdot \mathbf{c}_i \geq 0), \\ (1 - \chi)F_i^{\text{not}} + \chi F_i^{\text{bb}} & (-|\mathbf{c}_i| \sin \alpha_b \leq \mathbf{n}_k \cdot \mathbf{c}_i < 0), \\ F_i^{\text{bb}} & (\mathbf{n}_k \cdot \mathbf{c}_i < -|\mathbf{c}_i| \sin \alpha_b). \end{cases} \quad (17)$$

Here, F_i^{not} denotes the PDFs that pass through the boundary without the bounce-back condition, and F_i^{bb} denotes the PDFs that bounce back from the boundary with the bounce-back condition

$$F_i^{\text{not}} = f_i^{**}(\mathbf{X}_k, t + \Delta t), \quad (18)$$

$$F_i^{\text{bb}} = f_i^{**}(\mathbf{X}_k, t + \Delta t) + 6E_i \mathbf{c}_i \cdot \mathbf{U}_k, \quad (19)$$

where \bar{i} is the integer such that $\mathbf{c}_{\bar{i}} = -\mathbf{c}_i$. The angle α_b is the range where the present relaxation is applied, and the parameter χ is the relaxation coefficient, which is determined such that the bounce-back condition is relaxed continuously according to the normal vector \mathbf{n}_k as follows:

$$\chi = \frac{|\mathbf{n}_k \cdot \mathbf{c}_i|}{|\mathbf{c}_i| \sin \alpha_b}. \quad (20)$$

In the present study, we set $\alpha_b = 22.5^\circ$. If the angle α_b is too small, spurious oscillation of the local force will occur in the same way as in the original method. In fact, the present method tends to the original method as $\alpha_b \rightarrow 0$. If the angle α_b is too large, then the PDFs F_i^{not} that pass through the boundary will be much larger than the PDFs F_i^{bb} that bounce back from the boundary, and therefore the no-slip boundary condition will not be enforced appropriately. Therefore, the angle α_b must be determined by a balance between the above two situations. The dependence of the relaxation range α_b is discussed further in Appendix B.

The stress tensors $\sigma^{[1]}(\mathbf{X}_k)$ and $\sigma^{[2]}(\mathbf{X}_k)$ at a boundary Lagrangian point \mathbf{X}_k in fluids #1 and #2, respectively, are obtained using Eq. (5) as follows:

$$\sigma_{\alpha\beta}^{[\ell]} = -\frac{1}{2\tau} p^{[\ell]} \delta_{\alpha\beta} - \frac{\tau - \frac{1}{2}}{\tau} \left[\sum_{i=1}^b f_i^{[\ell]} (c_{i\alpha} - U_{k\alpha})(c_{i\beta} - U_{k\beta}) - (3p^{[\ell]} - 1)U_{k\alpha}U_{k\beta} \right] \quad (\ell = 1, 2), \quad (21)$$

where $p^{[\ell]}$ is the pressure in fluid ℓ calculated from Eq. (3) using $f_i^{[\ell]}$, and $U_{k\alpha}$ is the α component of the velocity \mathbf{U}_k of a boundary Lagrangian point.

The volume force is determined by the discontinuity in the stress tensor as follows:

$$\mathbf{g}(\mathbf{X}_k, t + \Delta t) \Delta V = -[\boldsymbol{\sigma}^{[1]}(\mathbf{X}_k) - \boldsymbol{\sigma}^{[2]}(\mathbf{X}_k)] \cdot \mathbf{n}_k \Delta S, \quad (22)$$

where ΔS is a small area element given by S/N , with S being the area of the body surface. In this method, we choose N such that $\Delta S \lesssim (\Delta x)^{d-1}$. In addition, the volume force is not added to one boundary Lagrangian point, but to a small volume element whose volume is denoted by ΔV . In this method, ΔV is taken as $\Delta S \times \Delta x$.

The volume force is distributed on lattice points around the boundary as follows:

$$\mathbf{g}(\mathbf{x}, t + \Delta t) = \sum_{k=1}^N \mathbf{g}(\mathbf{X}_k, t + \Delta t) W(\mathbf{x} - \mathbf{X}_k) \Delta V, \quad (23)$$

where the same weighting function (14) as in the interpolation (13) is used. Finally, the PDF is corrected by the volume force in Eq. (8) as follows:

$$f_i(\mathbf{x}, t + \Delta t) = f_i^{**}(\mathbf{x}, t + \Delta t) + 3\Delta x E_i c_i \cdot \mathbf{g}(\mathbf{x}, t + \Delta t). \quad (24)$$

D. Force and torque acting on the boundary from the external fluid

Suppose that fluid #1 is the external fluid outside the boundary. Then, the stress $\mathbf{P}(\mathbf{X}_k)$ acting on the boundary from the external fluid around a Lagrangian point \mathbf{X}_k is calculated as

$$\mathbf{P}(\mathbf{X}_k) = \boldsymbol{\sigma}^{[1]}(\mathbf{X}_k) \cdot \mathbf{n}_k. \quad (25)$$

Therefore, the total force acting on the boundary from the external fluid is given by

$$\mathbf{F} = \sum_{k=1}^N \mathbf{P}(\mathbf{X}_k) \Delta S. \quad (26)$$

In addition, the total torque around a point \mathbf{X}_c (e.g., the center of mass of a body) acting on the boundary from the external fluid is given by

$$\mathbf{T} = \sum_{k=1}^N (\mathbf{X}_k - \mathbf{X}_c) \times \mathbf{P}(\mathbf{X}_k) \Delta S. \quad (27)$$

E. Algorithm of computation

The algorithm of computation by the present numerical method is summarized as below.

0. Suppose the initial values of macroscopic variables $\mathbf{u}(\mathbf{x}, 0)$ and $p(\mathbf{x}, 0)$, and give the initial value of the PDF $f_i(\mathbf{x}, 0)$ by the equilibrium PDF (2) using these macroscopic variables. Also, assign the initial values of the total force $\mathbf{F}(0)$ and torque $\mathbf{T}(0)$ acting on the boundary.
1. Determine the position $\mathbf{X}_k(t + \Delta t)$, velocity $\mathbf{U}_k(t + \Delta t)$, and unit normal vector $\mathbf{n}_k(t + \Delta t)$ of the boundary Lagrangian

points. Also, determine the velocity $\mathbf{U}_{in}(\mathbf{x})$ of the body at a lattice point \mathbf{x} inside the boundary. (If the boundary is the surface of a body in free motion, they are determined by solving the equation of motion of the body.)

2. Compute the temporary PDFs $f_i^*(\mathbf{x}, t + \Delta t)$ by Eq. (7) and compute the temporary flow velocity $\mathbf{u}^*(\mathbf{x}, t + \Delta t)$ by Eq. (4).
3. Compute the preprocessing volume force $\mathbf{g}_p(\mathbf{x}, t + \Delta t)$ by Eq. (11), and compute the corrected temporary PDFs $f_i^{**}(\mathbf{x}, t + \Delta t)$ by Eq. (12).
4. Interpolate the corrected temporary PDFs $f_i^{**}(\mathbf{X}_k, t + \Delta t)$ on the boundary Lagrangian points by Eq. (13).
5. Compute the desired PDFs $f_i^{[1]}$ and $f_i^{[2]}$ by Eqs. (16) and (17), respectively.
6. Compute the stress tensors $\boldsymbol{\sigma}^{[1]}(\mathbf{X}_k, t + \Delta t)$ and $\boldsymbol{\sigma}^{[2]}(\mathbf{X}_k, t + \Delta t)$ by Eq. (21), and compute the total force $\mathbf{F}(t + \Delta t)$ and torque $\mathbf{T}(t + \Delta t)$ acting on the boundary by Eqs. (26) and (27), respectively.
7. Compute the volume force $\mathbf{g}(\mathbf{X}_k, t + \Delta t)$ on the boundary Lagrangian points by Eq. (22).
8. Distribute the volume force $\mathbf{g}(\mathbf{x}, t + \Delta t)$ on the lattice points by Eq. (23).
9. Compute $f_i(\mathbf{x}, t + \Delta t)$ by Eq. (24), and $p(\mathbf{x}, t + \Delta t)$ and $\mathbf{u}(\mathbf{x}, t + \Delta t)$ by Eqs. (3) and (4), respectively.
10. Advance one time step and return to 1.

III. NUMERICAL VALIDATION

In this section, we examine the accuracy of the present IB-LBM with relaxation of the bounce-back condition by applying it to simulations of two- and three-dimensional flows with stationary or moving boundaries, namely, flow over a stationary circular cylinder, an oscillating circular cylinder in a stationary fluid, particle migration in a plane Couette flow, and sedimentation of a sphere. In the following, the *original method* denotes the stress tensor discontinuity-based IB-LBM with preprocessing by the SPM proposed in Ref. 14, and the *present method* denotes the method in which relaxation of the bounce-back condition is applied to the original method.

A. Flow over a stationary circular cylinder

First, we consider a well-known benchmark problem of flow over a stationary circular cylinder. The diameter of the circular cylinder is D , the computational domain is $[-16D, 24D] \times [-20D, 20D]$, and the center of the circular cylinder is located at $(x, y) = (0, 0)$. The pressure and velocity on all of the outer boundaries of the computational domain are imposed as $p = p_\infty$ and $\mathbf{u} = (u_\infty, 0)$, where p_∞ and u_∞ are constant. We assume that the unknown PDFs on the outer boundaries are equal to the equilibrium PDFs with the pressure and velocity on the outer boundaries. The pressure and velocity are initially set to be uniform, with the same values as those in the boundary conditions. The governing parameter of the system is the Reynolds number, defined as $Re = u_\infty D / \nu$. In this simulation, we set $D = 50\Delta x$, $N = 204$, $p_\infty = 1/3$, and $u_\infty = 0.03$.

Figure 4 shows the streamlines around the circular cylinder at $Re = 40$ when the flow reaches a steady state. We can see that the original method and the present method give almost the same flow fields without penetration of the streamline across the boundary. The preprocessing by the SPM (see Sec. II B) prevents penetration. The effect

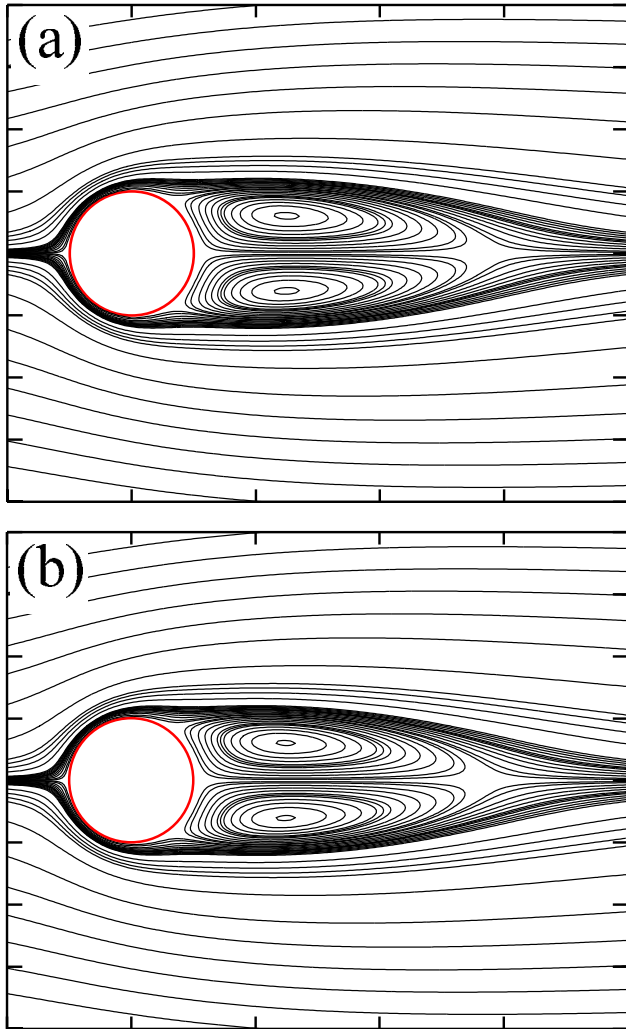


FIG. 4. Streamlines in the flow past a circular cylinder at $Re = 40$ for (a) the original method [taken from Fig. 10(b) in Ref. 14] and (b) the present method. (a) Reprinted with permission from Suzuki and Yoshino, *Comput. Fluids* **172**, 593–608 (2018). Copyright 2018 Elsevier Ltd.

of the relaxation of the bounce-back condition in the present method cannot be observed in terms of the flow field.

We calculate the pressure and skin-friction coefficients at a boundary Lagrangian point with argument θ defined by

$$C_p(\theta) = \frac{p^{[1]}(\theta) - p_{\text{ref}}}{0.5\rho_f u_{\text{ref}}^2}, \quad (28)$$

$$C_f(\theta) = \frac{\mathbf{t}(\theta)^T \boldsymbol{\sigma}^{[1]}(\theta) \mathbf{n}(\theta)}{0.5\rho_f u_{\text{ref}}^2}, \quad (29)$$

where $p^{[1]}$ is the pressure on the boundary point calculated using $f_i^{[1]}$ (see Sec. II C), supposing that fluid #1 is the external fluid. The vectors \mathbf{n} and \mathbf{t} are respectively the unit normal and tangential vectors on the boundary, and superscript T denotes the transpose of a vector. p_{ref} is

the reference pressure, and u_{ref} is the reference flow speed. In this problem, we set $p_{\text{ref}} = p_{\infty}$ and $u_{\text{ref}} = u_{\infty}$.

Figure 5 shows the pressure coefficient C_p and the skin-friction coefficient C_f on the circular cylinder at $Re = 40$. We can see that the results from the original method exhibit the spurious oscillation around $\theta = 45^\circ$ and 90° . On the other hand, the results from the present method have no spurious oscillation and are in good agreement with other numerical results.^{33–35} These results mean that the relaxation of the bounce-back condition is effective in preventing spurious oscillation of the local force along the boundary.

Table I shows the drag coefficient defined by $C_D = 2F_x/(\rho_f u_{\infty}^2 D)$ (where F_x is the force acting on the body in the direction parallel to the inflow) and the wake length L_w/D (where L_w is the length of the recirculation region from the rearmost point of the cylinder to the end of the wake), together with other experimental^{36,37} and numerical^{22,33,38,39} results for $Re = 20$ and 40. We can see that the results not only from the present method but also from the original

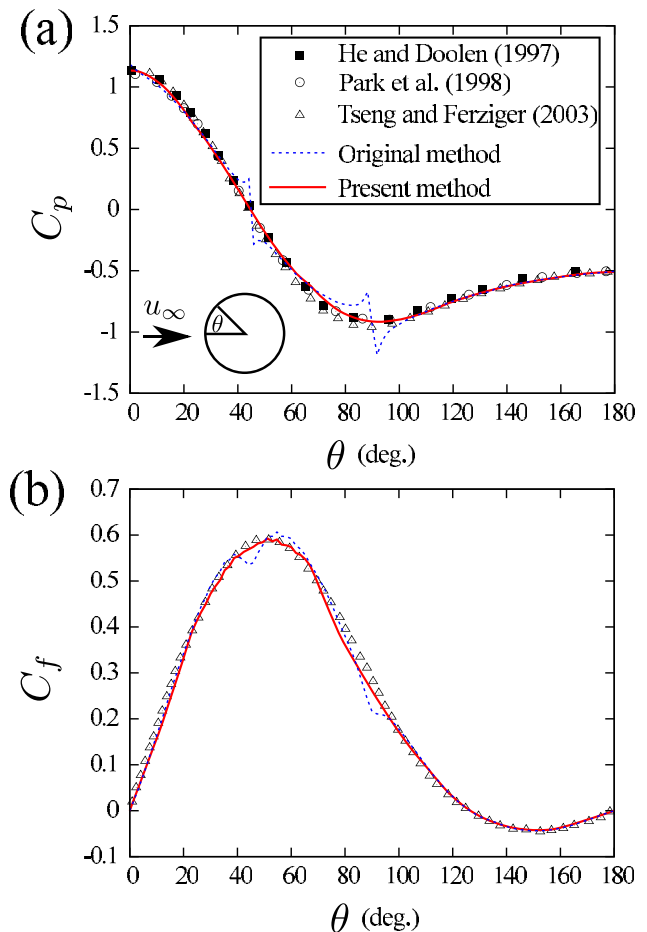


FIG. 5. Distributions of (a) the pressure coefficient C_p and (b) the skin-friction coefficient C_f on the circular cylinder in a uniform flow at $Re = 40$. The numerical results from the present method and the original method¹⁴ are shown, together with the numerical results obtained by He and Doolen,³³ Park et al.,³⁴ and Tseng and Ferziger.³⁵

TABLE I. Comparison of the drag coefficient C_D and the wake length L_w/D at $Re = 20$ and 40.

Re	References	C_D	L_w/D
20	Tritton ³⁶ (Expt.)	2.09	...
	Coutanceau and Bouard ³⁷ (Expt.)	...	0.93
	Dennis and Cheng ³⁸	2.045	0.94
	He and Doolen ³³	2.152	0.921
	Taira and Colonius ³⁹	2.07	0.94
	Wu and Shu ²²	2.091	0.93
	Original ¹⁴	2.071	0.96
	Present	2.064	0.96
40	Tritton ³⁶ (Expt.)	1.59	...
	Coutanceau and Bouard ³⁷ (Expt.)	...	2.13
	Dennis and Cheng ³⁸	1.522	2.35
	He and Doolen ³³	1.550	2.25
	Taira and Colonius ³⁹	1.54	2.30
	Wu and Shu ²²	1.565	2.31
	Original ¹⁴	1.548	2.34
	Present	1.542	2.34

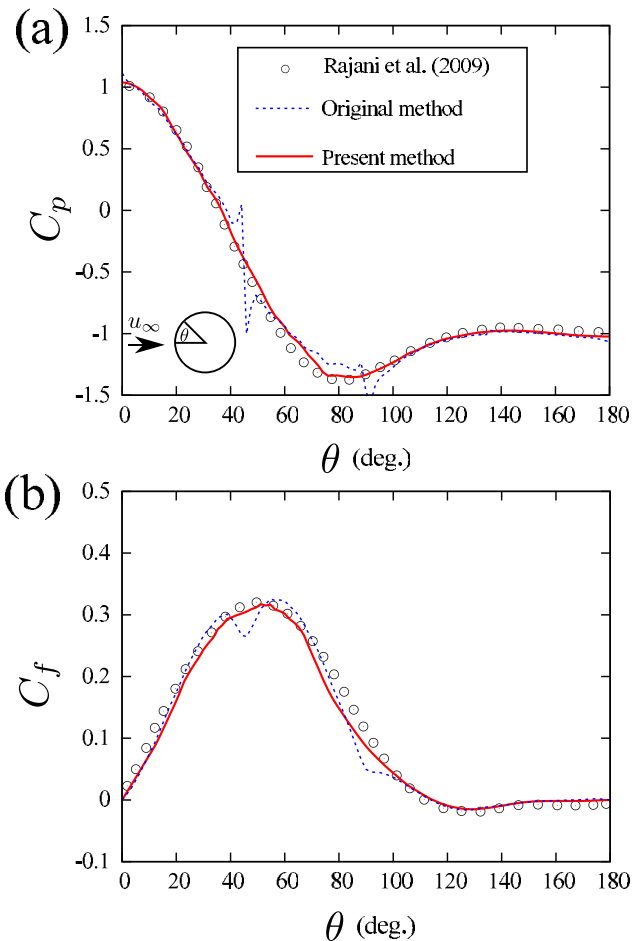
method agree well with the other results. This suggests that the spurious oscillation of the local force has a small effect on the net force and the external flow field.

To examine whether the relaxation of the bounce-back condition is effective for unsteady flows at a higher Reynolds number, we calculate C_p and C_f for $Re = 200$, at which vortex shedding occurs. Figure 6 shows the time-averaged distributions of C_p and C_f which are averaged during 30 periods of the vortex shedding after it becomes periodic. We can see that the present method can effectively prevent the spurious oscillation of the local force along the boundary even for unsteady flows, and the present results show good agreement with the other numerical results.⁴⁰ Table II shows the drag coefficient C_D defined as above, the lift coefficient defined by $C_L = 2F_y/(\rho_f u_\infty^2 D)$ (where F_y is the force acting on the body in the direction perpendicular to the inflow), and the Strouhal number $St = f_s D_s / u_\infty$ of the vortex shedding (where f_s is the shedding frequency), together with other experimental⁴¹ and numerical^{39,42–44} results. We can see that the results not only from the present method but also from the original method agree well with the other results. Therefore, the same conclusions can be drawn as for steady flows at $Re = 20$ and 40.

B. Translationally oscillating circular cylinder in a stationary fluid

Second, we consider an oscillating circular cylinder in a stationary fluid. This problem was studied both experimentally and numerically by Dütsch *et al.*⁴⁵ The diameter of the cylinder is D , and the width and the height of the computational domain are $55D$ and $35D$, respectively. The fluid is initially at rest, and the cylinder, placed at the center of the domain, suddenly starts to oscillate with speed,

$$U_c(t) = -U_{\max} \cos\left(\frac{2\pi}{T}t\right), \quad (30)$$


FIG. 6. Time-averaged distributions of (a) the pressure coefficient C_p and (b) the skin-friction coefficient C_f on a circular cylinder in a uniform flow for $Re = 200$. The numerical results from the present method and the original method¹⁴ are shown, together with the numerical results obtained by Rajani *et al.*⁴⁰

$$V_c(t) = 0, \quad (31)$$

where $U_c(t)$ and $V_c(t)$ are the respective velocity components in the x and y directions of the cylinder, U_{\max} is the amplitude of the velocity,

TABLE II. Comparison of drag coefficient C_D , lift coefficient C_L , and Strouhal number St of vortex shedding at $Re = 200$.

References	C_D	C_L	St
Roshko ⁴¹ (Expt.)	0.19
Liu <i>et al.</i> ⁴²	1.31 ± 0.049	± 0.69	0.192
Linnick and Fasel ⁴³	1.34 ± 0.044	± 0.69	0.197
Taira and Colonius ³⁹	1.35 ± 0.048	± 0.68	0.196
Wang <i>et al.</i> ⁴⁴	1.43 ± 0.051	± 0.75	0.195
Original ¹⁴	1.39 ± 0.050	± 0.73	0.195
Present	1.37 ± 0.050	± 0.71	0.195

and T is the period. In the simulation, the diameter of the circular cylinder is $D = 50\Delta x$, and the number of boundary Lagrangian points along the cylinder surface is $N = 204$. A Neumann boundary condition is imposed on the outer boundary of the domain, i.e., $\mathbf{n}_d \cdot \nabla \mathbf{f}_i = 0$ (where \mathbf{n}_d is the unit vector normal to the boundary). The governing parameters of the system are the Reynolds number $Re = U_{\max} D / \nu$ and the Keulegan–Carpenter number $KC = 2\pi A_m / D$, where A_m is the spatial amplitude of the oscillation. We consider the case $Re = 100$ with $KC = 5$. In this simulation, we set $U_{\max} = 0.03$ and $\tau = 0.5450$.

Figure 7 shows the time variation of the drag coefficient $C_D = 2F_x / (\rho_f U_{\max}^2 D)$. The contributions from the pressure and the shear stress to C_D are also shown. It should be noted that since the results by Dütsch *et al.*⁴⁵ are for periods after initial transient flows, we cut off the transients for the first period ($0 \leq t/T < 1$) of our results. Hence, the data in Fig. 7 begin with the second period.

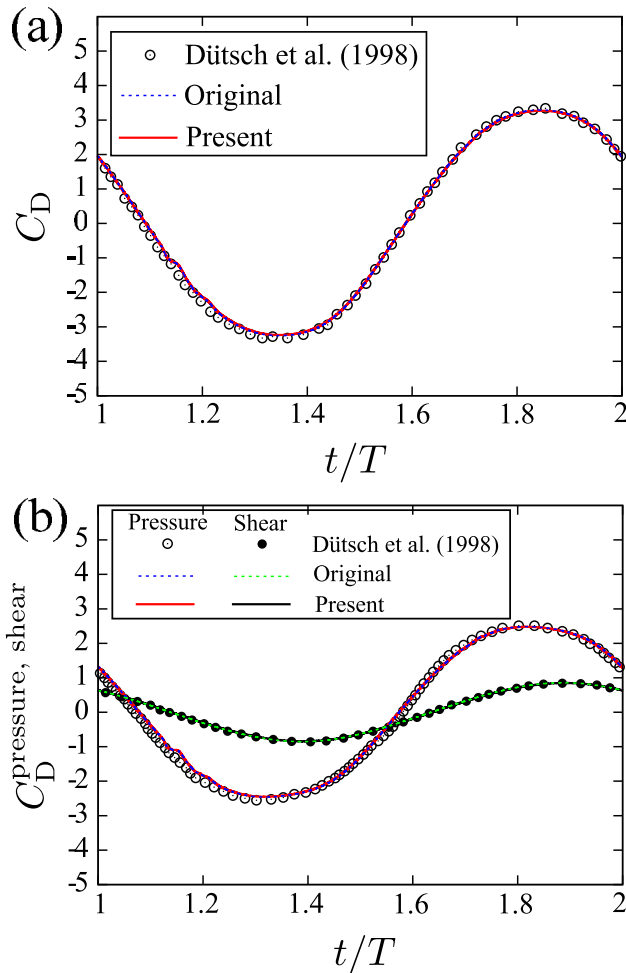


FIG. 7. Time variations of (a) the drag coefficient C_D and (b) the contributions from the pressure and the shear stress to C_D of a translationally oscillating circular cylinder for $Re = 100$ with $KC = 5$. The results obtained from the present method are compared with the numerical results from the original method¹⁴ and those by Dütsch *et al.*⁴⁵

We can see from Fig. 7 that the results from the present method almost coincide with those from the original method¹⁴ and that these results quantitatively agree with the numerical results by Dütsch *et al.*⁴⁵ in terms of both the total force and the contributions from the pressure and shear stress. This means that both the present and original methods can give an accurate force acting on a moving body not in terms of the local force but in terms of the net force. In addition, by using the stress tensor discontinuity-based IB-LBM, we can accurately separate the net force into the contributions from the pressure and from the shear stress. This is one of the advantages of the stress tensor discontinuity-based IB-LBM.

In this problem, unfortunately, we could not find any data about the local force. In our preliminary computation, the local force obtained using the original method had a large spurious oscillation along the boundary, whereas the local force obtained using the present method did not (see also the red line in Fig. 8). Therefore, the present method gives more accurate results for the local force than the original method, although they give almost the same net force. This is

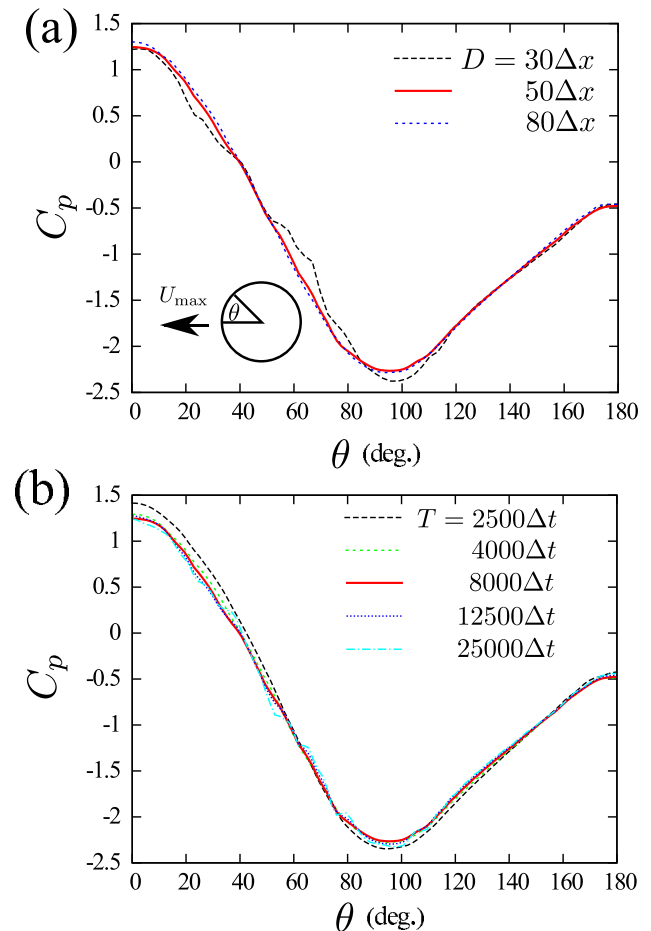


FIG. 8. Distributions of the pressure coefficient C_p on a translationally oscillating circular cylinder at $t/T = 2.0$: (a) with various spatial resolutions for $T = 8000\Delta t$; (b) with various time resolutions for $D = 50\Delta x$.

consistent with the results for flow over a stationary circular cylinder in Sec. III A.

Here, we check the robustness of the present method with various space and time resolutions. The computational parameters are shown in Table III. Figure 8 shows the pressure coefficient C_p given by Eq. (28) for $p_{\text{ref}} = 1/3$ (initial pressure) and $u_{\text{ref}} = U_{\text{max}}$. We can see from Fig. 8(a) that the results for $D = 50\Delta x$ and $80\Delta x$ are smooth and almost coincident with each other. However, the result for $D = 30\Delta x$ is rugged and significantly different from the results for higher spatial resolutions. This is not because the spatial resolution is insufficient for $D = 30\Delta x$ but because the relaxation time is so small and close to 0.5. Actually, in our preliminary computation, the result for $D = 30\Delta x$ and $\tau = 0.5338$ was not rugged. This harmful effect of a small relaxation time can also be found in Fig. 8(b), which shows the dependence of the time resolution. We can see from this figure that the result for $T = 25000\Delta t$ is somewhat rugged due to the small relaxation time, whereas the results for lower time resolutions are not rugged. In addition, we can see that the results for $T = 4000\Delta t$, $8000\Delta t$, and $12500\Delta t$ agree well with each other, whereas the result for $T = 2500\Delta t$ is significantly different from the results for higher time resolutions. This is because for $T = 2500\Delta t$ the maximum flow velocity U_{max} is so large that the flow field can violate the condition that the Mach number $Ma \ll 1$. In this case, the effect of compressibility cannot be neglected. These results suggest that we should set the relaxation time to be $\tau \gtrsim 0.53$ and the maximum flow speed to be $U_{\text{max}} \lesssim 0.06$ to obtain reasonable local force acting on the boundary by the present method. It should be noted that the total force is almost identical for all space and time resolutions except the case where the condition that $Ma \ll 1$ is violated.

C. Particle migration in plane Couette flow

Third, we consider the migration of a circular cylinder in a simple shear flow. This problem was studied by Feng *et al.*⁴⁶ using a finite element simulation. The diameter of the cylinder is D , and its density is the same as that of the fluid, i.e., it is neutrally buoyant. The size of the computational domain is $L \times H = 4D \times 4D$, and the top and bottom walls move in opposite directions with speed $u_w/2$ (see Fig. 9), and thus Couette flow is induced in the domain. The periodic boundary condition is applied at the inlet and outlet of the domain. We set the Reynolds number $Re = u_w H / \nu = 40$.

TABLE III. Computational parameters to check the robustness of the present method with various space and time resolutions for a translationally oscillating circular cylinder, where D is the diameter of the cylinder, T is the period of the oscillation, U_{max} is the amplitude of the velocity, and τ is the relaxation time.

D	T	U_{max}	τ
$30\Delta x$	$8000\Delta t$	0.01875	0.5169
$50\Delta x$	$8000\Delta t$	0.03125	0.5469
$80\Delta x$	$8000\Delta t$	0.05000	0.6200
$50\Delta x$	$2500\Delta t$	0.1000	0.6500
$50\Delta x$	$4000\Delta t$	0.0625	0.5938
$50\Delta x$	$12500\Delta t$	0.0200	0.5469
$50\Delta x$	$25000\Delta t$	0.0100	0.5150

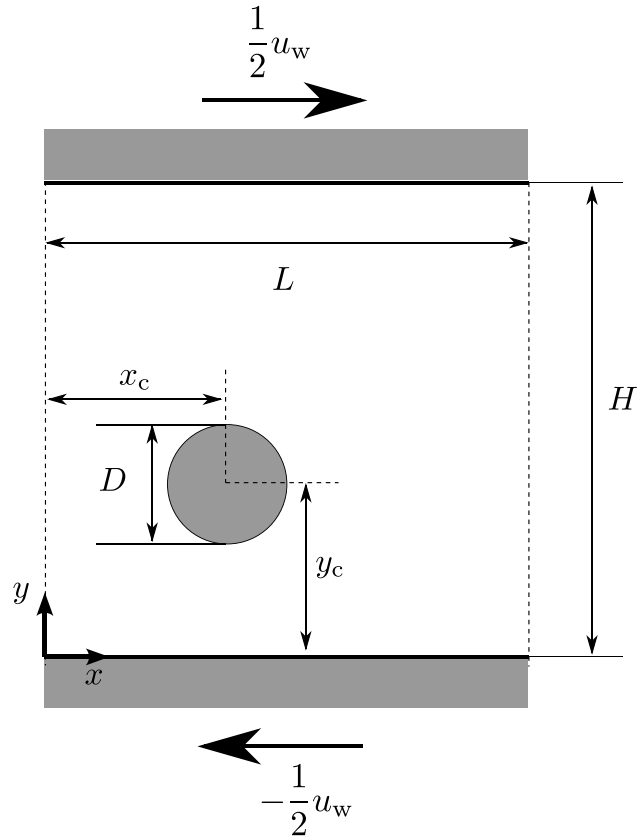


FIG. 9. Computational domain for the migration of a particle in plane Couette flow.

The fluid and the circular cylinder are initially at rest. The fluid starts to move owing to the moving top and bottom walls, and the circular cylinder starts to move owing to the force and torque imposed on it by the fluid. We compute the translational and rotational equations of motion of the circular cylinder using the second-order Adams–Bashforth method. In this simulation, we set $D = 50\Delta x$, $N = 204$, and $u_w = 0.03$.

Figure 10 shows the time variations of the lateral position y_c of the circular cylinder for various initial positions. We can see that the results from the present method almost coincide with those from the original method. This means that the relaxation of the bounce-back condition has a small effect on the net force and on the motion of the body. In addition, the lateral position of the circular cylinder tends to the centerline between the top and bottom walls as time advances, independently of the initial position. This motion can be seen in the results by Feng *et al.*,⁴⁶ and therefore the present results can be regarded as reasonable.

Figure 11 shows the pressure coefficient C_p and the skin-friction coefficient C_f given by Eqs. (28) and (29) for $p_{\text{ref}} = 1/3$ (initial pressure) and $u_{\text{ref}} = u_w$. We can see that the results from the original method exhibit the spurious oscillation around $\theta = 45^\circ, 90^\circ, 135^\circ, \dots$, and 315° . On the other hand, the results from the present method have no spurious oscillation and are in good agreement with the other numerical results.⁴⁶ Therefore, the relaxation of the bounce-

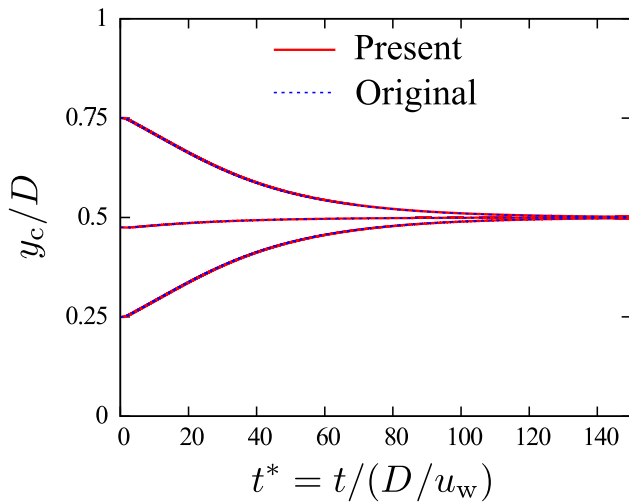


FIG. 10. Time variations of the lateral position y_c of a circular cylinder in plane Couette flow for various initial positions for the present method and the original method.¹⁴

back condition can effectively eliminate the spurious oscillation of the local force along the boundary, even for moving-boundary flows.

D. Sedimentation of a sphere

Finally, we consider a sphere falling under gravity in a closed box filled with fluid. This problem was investigated using particle image velocimetry (PIV) by ten Cate *et al.*⁴⁷ The experimental conditions are presented below in terms of dimensional variables. The dimensions of the box are depth \times width \times height = 100 mm \times 100 mm \times 160 mm. The diameter of the sphere is $\hat{D}_p = 15$ mm, and its density is $\hat{\rho}_b = 1120$ kg/m³. The fluid is initially at rest, and the sphere starts its motion due to gravitational acceleration $\hat{g} = 9.8$ m/s² at a height 120 mm from the bottom of the domain. In the simulation, the domain is divided into a $200 \times 200 \times 320$ lattice grid. Hence, 30 lattice spacings are used for the diameter of the sphere. The boundary Lagrangian points on the sphere should be arranged uniformly and symmetrically. In the present study, we use a spherical geodesic grid with refinement loop $n = 5$.⁴⁸ The number of boundary Lagrangian points is $N = 10\,242$. The bounce-back condition¹⁶ is used to enforce the no-slip condition on the outer boundary of the box. The governing parameters of the system are the density ratio of the sphere to the fluid $\gamma = \hat{\rho}_b/\hat{\rho}_f$ and the Reynolds number $Re = \hat{\rho}_f \hat{u}_\infty \hat{D}_p/\hat{\mu}$, where \hat{u}_∞ is the sedimentation velocity of a sphere in an infinite domain⁴⁷ and $\hat{\mu}$ is the fluid viscosity.

We calculate four cases as listed in Table IV. The simulated results for the gap L and the falling velocity u are shown in Fig. 12, together with the experimental results by ten Cate *et al.*⁴⁷ We can see that the results from the present method almost coincide with those from the original method. This means that the relaxation of the bounce-back condition has a small effect on the net force and on the motion of the body. In addition, the present results agree reasonably well with the experimental results by ten Cate *et al.*⁴⁷ for all four cases. This means that the present method can be successfully applied to three-dimensional moving-boundary flows.

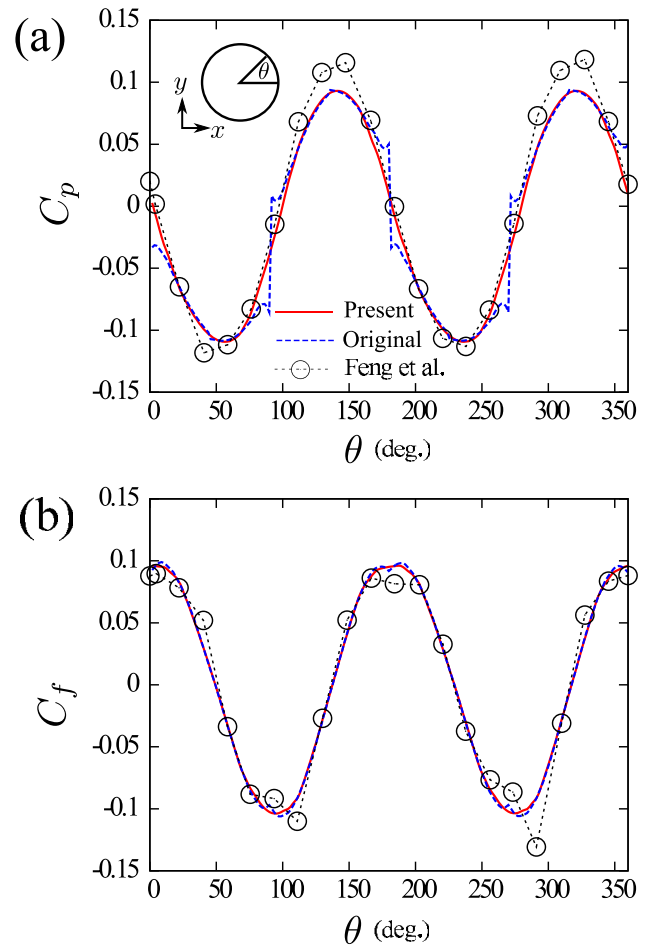


FIG. 11. Distributions of (a) the pressure coefficient C_p and (b) the friction coefficient C_f on a circular cylinder in plane Couette flow. The numerical results from the present method and the original method¹⁴ are shown, together with the numerical results by Feng *et al.*⁴⁶

We calculate the pressure coefficient C_p and the skin-friction coefficient C_f given by Eqs. (28) and (29) for $p_{\text{ref}} = 1/3$ (initial pressure) and $u_{\text{ref}} = u_\infty$. Figure 13 shows the distributions of C_p and C_f on an equator of the sphere for $Re = 32.2$ at $\hat{t} = 0.983$ s. In this problem, unfortunately, we could not find any data about the local force. Thus, this figure contains only the results from the original and present methods. We can see that the results from the original method

TABLE IV. Fluid properties in the experiment by ten Cate *et al.*⁴⁷ and the parameters used for simulations of the sedimentation of a sphere.

Re	$\hat{\rho}_f$ (kg/m ³)	$\hat{\mu}$ ($\times 10^{-3}$ N s/m ²)	τ	$g\Delta x$
1.5	970	373	0.8000	8.284×10^{-5}
4.1	965	212	0.8000	2.538×10^{-4}
11.6	962	113	0.7328	5.344×10^{-4}
32.2	960	58	0.5839	2.622×10^{-4}

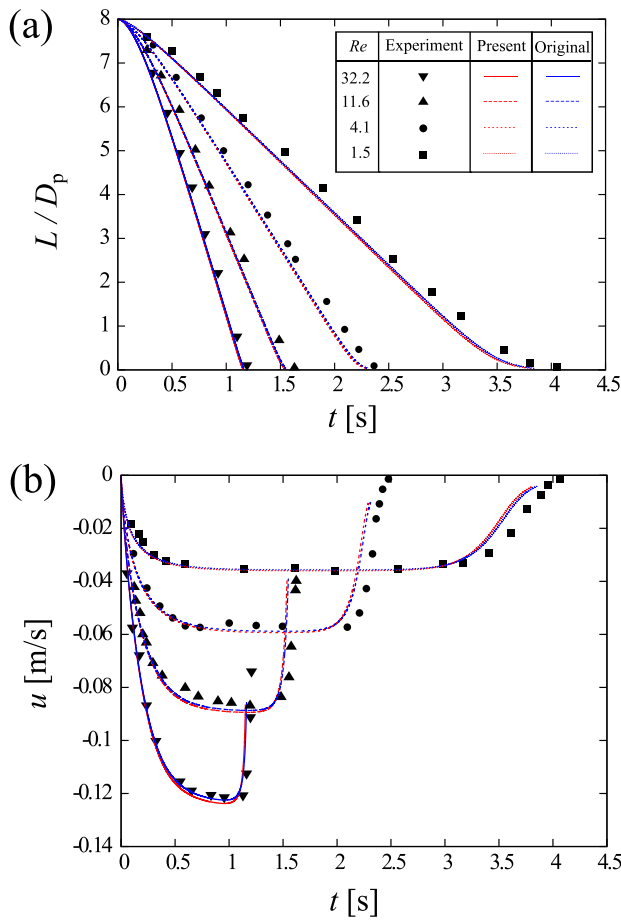


FIG. 12. Comparisons of results from the present method with experimental results by ten Cate *et al.*⁴⁷ for (a) the time variation of the gap L between the sphere and the bottom of the domain and (b) the time variation of the velocity of the sphere u .

exhibit a spurious oscillation as in the previous two-dimensional simulations, whereas the results from the present method have no spurious oscillation. Therefore, the relaxation of the bounce-back condition can effectively eliminate the spurious oscillation of the local force along the boundary, even for three-dimensional moving-boundary flows.

IV. APPLICATION: WING-WAKE INTERACTION ON A TWO-DIMENSIONAL BUTTERFLY-LIKE FLAPPING WING

In this section, we apply the present method to local force calculations on a two-dimensional butterfly-like flapping wing to investigate wing-wake interaction.

It has been supposed that one of the major causes of lift enhancement in insects is collision of their wings with the flow induced between vortex pairs separated from the wings⁴⁹ (*wing-wake interaction* or *wake capture*). However, it remains debatable whether insects utilize this wing-wake interaction for lift enhancement.⁵⁰ In addition, the effect of wing-wake interaction is likely to be strongly dependent on the species of insect and their flight mode. In particular, it was shown in an experiment using free-flying butterflies⁵¹ that wing-wake

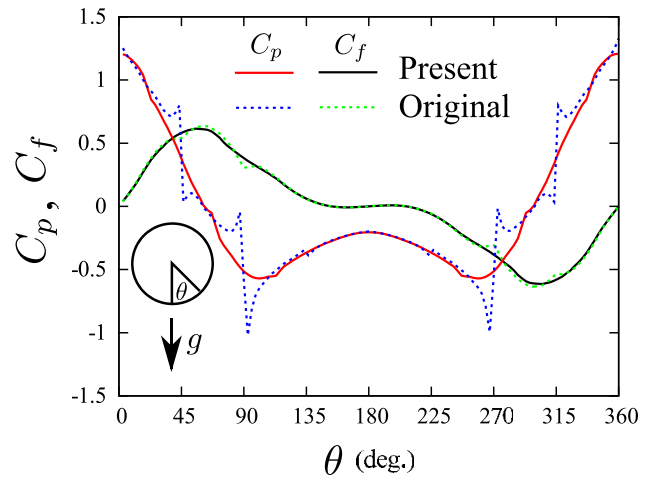


FIG. 13. Distributions of the pressure coefficient C_p and the skin-friction coefficient C_f on an equator of a sphere falling in a stationary fluid for $Re = 32.2$ at $t = 0.983$ s. The numerical results from the present method are compared with those from the original method.¹⁴

interaction was observed in some cases but not in others. Thus, the significance of wing-wake interaction for butterflies remains unclear.

To investigate the effect of wing-wake interaction on lift enhancement, we have to calculate the local force acting on the surface of the flapping wing. The difficulty of calculating this local force is likely to be one reason why the effect of wing-wake interaction has not previously been evaluated quantitatively. In the present study, using the proposed IB-LBM, we demonstrate a first evaluation of the effect of wing-wake interaction on lift enhancement for butterflies.

As a wing model representing a butterfly wing, we use the two-dimensional butterfly-like flapping wing model.⁵² The wing in this model is a thin elliptical cylinder with aspect ratio equal to 10. The length of the major axis of the wing is denoted by L . The center $X_c(t)$ of the wing moves in a figure-of-eight pattern, and the angle of attack $\alpha(t)$ of the wing changes such that the wing flaps downward and backward during downstroke and upstroke, respectively. The expressions for $X_c(t)$ and $\alpha(t)$ are

$$X_c = L \sin \theta_m \cos \left(\frac{2\pi}{T} t \right) \begin{bmatrix} \sin \alpha(t) \\ \cos \alpha(t) \end{bmatrix}, \quad (32)$$

$$\alpha(t) = -\frac{\alpha_m}{2} \left[1 + \cos \left(\frac{2\pi}{T} t + \frac{\pi}{2} \right) \right], \quad (33)$$

where $\theta_m = 45^\circ$ is the flapping amplitude, T is the period of flapping motion, and $\alpha_m = 90^\circ$ is the maximum angle of attack. The motion of the wing during one stroke can be seen in Fig. 14.

We should mention how to implement the preprocessing (see Sec. II B) for the elliptical cylinder. We set the radius R of the area where the preprocessing is applied to

$$R = \frac{ab}{\sqrt{(a \sin \psi)^2 + (b \cos \psi)^2}} - 0.5\Delta x, \quad (34)$$

where a and b are the long and short axial radii, respectively, and ψ is the angle from the line connecting the center and the leading edge of

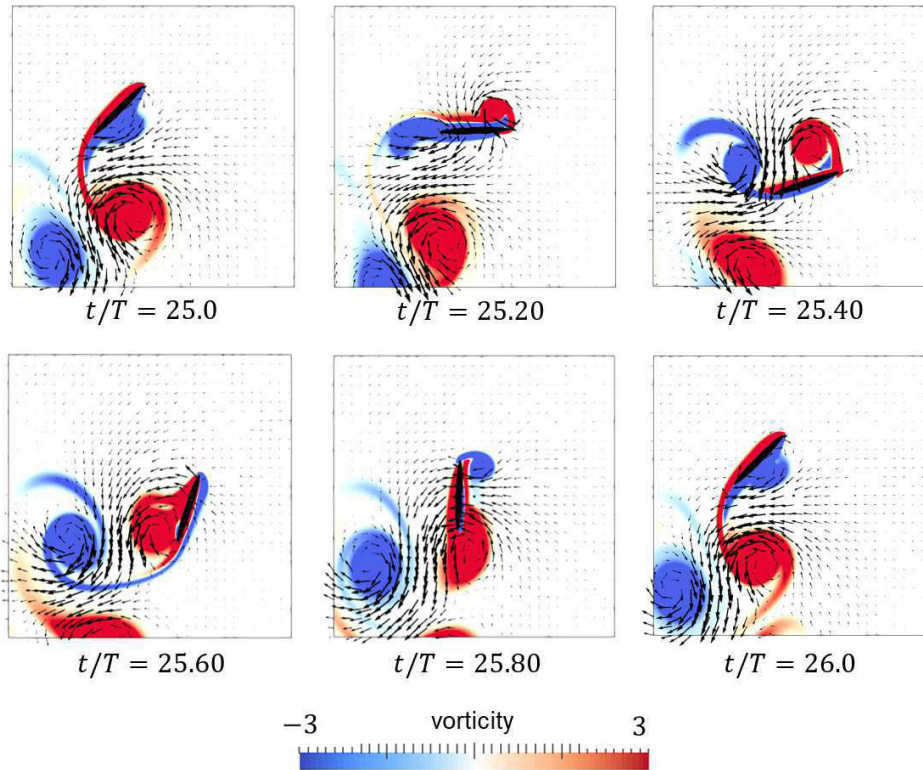


FIG. 14. Time variations of the vorticity and velocity fields around the wing model.

the elliptical cylinder. All other parts of the preprocessing are the same as for the circular cylinder.

The computational domain is square, with width equal to $32L$. There is no incoming flow, and a Neumann boundary condition is applied on the outer boundary of the domain. The center of the flapping motion is located at $(19.2L, 22.4L)$ to prevent the induced flow from interacting with the outer boundary of the domain. We set the length of the major axis (i.e., the wing-chord length) to $L = 90\Delta x$ and the period of the flapping motion to $T = 6000\Delta t$. The governing parameter of this system is the Reynolds number, given by $Re = UL/\nu$, where $U = 4L\theta_m/T$ is the mean flapping speed. In the present study, we set $Re = 100$.

Figure 14 shows the time variations of the vorticity and velocity fields during one stroke in the 25th period, where the flow field and the force acting on the wing are sufficiently periodic. The vorticity field is represented by the nondimensional vorticity defined by $\omega = (\partial v/\partial x - \partial u/\partial y)L/U$. We can see that during the downstroke ($25 \leq t/T \leq 25.5$), large vortices are formed around the leading and trailing edges of the wing and eventually separate from these edges. Like an actual butterfly⁵³ or a 3D butterfly-like flapping wing-body model,⁵⁴ the leading-edge vortex attached to the upper surface of the wing is considered to be a primary source of lift, since it induces a low-pressure region on the upper surface. This vortex pair induces downward flow and is convected downward in the next upstroke ($25.5 \leq t/T \leq 26$). Similarly, during the upstroke, a leading-edge vortex and a trailing-edge vortex are formed and separate, and this vortex pair induces backward flow and is convected backward in the next downstroke. In the same way as the downstroke, the leading-edge

vortex attached to the lower surface of the wing is considered to be a primary source of thrust.

Thus, the downstroke induces downward flow, and the upstroke induces backward flow. Some experiments and simulations using actual butterflies have observed similar downward and backward flows, which are induced by vortex rings separated from the wings.^{55,56} In terms of the wing-wake interaction, around $t/T = 25.3$, the wing collides with the backward flow induced in the previous upstroke, whereas around $t/T = 25.8$, the wing collides with the downward flow induced in the previous downstroke.

Figure 15 shows the local force acting on the wing surface and the vorticity, velocity, and pressure fields when the wing collides with the flow induced in the previous stroke. The local force is represented by the local lift coefficient C_L (nondimensional vertical force) and the local thrust coefficient C_T (nondimensional horizontal force) defined by

$$C_L(\theta) = \frac{\{[\sigma^{[1]}(\theta) - p_{\text{ref}}\mathbf{I}]\mathbf{n}(\theta)\}_y}{0.5\rho_f U^2}, \quad (35)$$

$$C_T(\theta) = \frac{\{[\sigma^{[1]}(\theta) - p_{\text{ref}}\mathbf{I}]\mathbf{n}(\theta)\}_x}{0.5\rho_f U^2}, \quad (36)$$

where p_{ref} is the reference pressure, \mathbf{I} is the identity matrix, and \mathbf{n} is the unit normal vector on the wing surface. It should be noted that we consider the gauge pressure in the above definitions.

We can see from Figs. 15(a) and 15(c) that at $t/T = 25.3$, the local lift coefficient C_L around $180^\circ \leq \theta \leq 270^\circ$ (where the wing collides with the backward flow induced in the previous upstroke) does

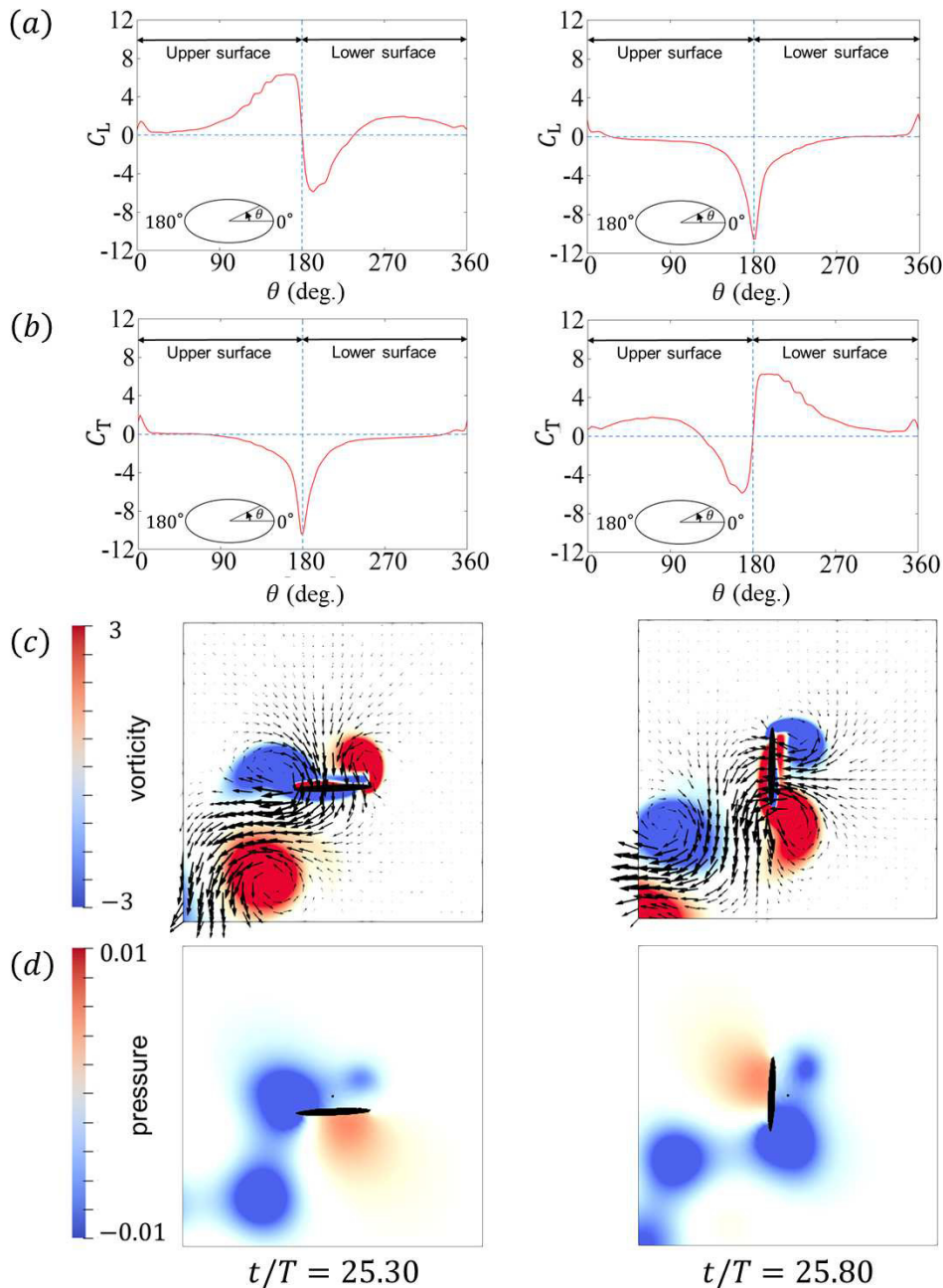


FIG. 15. (a) Local lift coefficient C_L , (b) local thrust coefficient C_T , (c) vorticity and velocity fields, and (d) pressure field at $t/T = 25.30$ and 25.80 for $Re = 100$.

not show any lift enhancement. This can be attributed to the fact that the induced flow is almost parallel to the wing surface when they collide with each other. The distribution of C_L seems to be affected not by the flow field but by the pressure field, as shown in Fig. 15(d). The negative pressure around the trailing edge is generated by the trailing-edge vortex, and the positive pressure around $270^\circ \leq \theta \leq 360^\circ$ is generated by the collision between the wing and the fluid at rest. We can see from Figs. 15(b) and 15(c) that, similarly to C_L , at $t/T = 25.8$, the local thrust coefficient C_T around $90^\circ \leq \theta \leq 180^\circ$ (where the wing

collides with the downward flow induced in the previous downstroke) does not show any thrust enhancement. Therefore, wing-wake interaction does not affect lift or thrust enhancement for the two-dimensional butterfly-like flapping wing model.

This result suggests that wing-wake interaction is not significant for the flapping flight of butterflies. Although the present model is highly idealized, real butterflies also induce downward and backward flows during downstroke and upstroke, respectively,^{55,56} in the same way as the present model. Thus, it can be expected that even in the

free flight of real butterflies, neither local lift nor thrust forces are enhanced on the part of the wing surface colliding with the flow induced in the previous stroke. This can be examined by applying the present method to a three-dimensional butterfly model. We leave this for future work.

V. CONCLUSIONS

We have improved the stress tensor discontinuity-based IB-LBM by relaxing the bounce-back condition. In the original stress tensor discontinuity-based IB-LBM, a spurious oscillation of the local force along the boundary appears near the boundary points where their normal vectors on the boundary are parallel or inclined by 45° to the grid lines. In the present study, we have identified the cause of this spurious oscillation as the fact that the set of desired particle distribution functions that are given by the bounce-back condition can be suddenly changed along the boundary. To avoid such a sudden change, we have considered relaxation of the bounce-back condition.

To confirm the improvement achieved, we have applied the new method to simulations of typical benchmark problems involving two- and three-dimensional flows with stationary or moving boundaries, namely, flow over a stationary circular cylinder, an oscillating circular cylinder in a stationary fluid, particle migration in plane Couette flow, and sedimentation of a sphere. The simulations show that the present method can eliminate spurious oscillation in the local force effectively, and the results obtained agree well with other numerical results. Thus, it is shown that the present method can give reasonable local force acting on the boundary in the framework of the diffuse-interface scheme. The local force calculation without using the normal probe approach^{12,13} has not been achieved by any other diffuse-interface scheme, but the present method makes it possible by calculating the stress tensor on the boundary Lagrangian points from the desired PDFs given by the relaxed bounce-back condition.

In addition, as an application of the present method to local force calculation, we have investigated the effect of lift enhancement due to wing-wake interaction on a two-dimensional butterfly-like flapping wing, which is a thin elliptical cylinder flapping downward and backward during downstroke and upstroke, respectively. Although the wing-wake interaction has been considered as a major cause of lift enhancement in the flapping flight of butterflies, it has not been quantitatively evaluated due to the absence of simple tools for calculating the local force acting on the surface of flapping wings. The present method can successfully give the local lift and thrust forces acting on the wing, and the results show that neither local lift nor thrust forces are enhanced by collision between the wing and the flow induced in its previous stroke. This suggests that wing-wake interaction is not significant for the flapping flight of butterflies. Also, this demonstration shows that the present method can give more detailed information in fluid-structure interaction than conventional diffuse-interface schemes.

Finally, we suggest some future directions for investigating the present method. It can give the force locally acting on the boundary in the framework of the diffuse-interface scheme. Therefore, it should be applicable to problems where computation of the local force is essential, such as those involving deformable particles and walls. In addition, the present method might be combined with the free surface-lattice Boltzmann method⁵⁷ to allow consideration of the motion of a solid body in a gas-liquid two-phase flow, for which the

local forces applied by the gas and liquid phases have to be computed separately. The extension of the present method in these directions remains a goal for future work.

ACKNOWLEDGMENTS

This work was partially supported by JSPS KAKENHI Grant No. JP19K14885.

APPENDIX A: NONDIMENSIONAL VARIABLES

In Sec. II, we use the following nondimensional variables defined by a characteristic length \hat{H}_0 , a characteristic particle speed \hat{c} , a characteristic timescale $\hat{t}_0 = \hat{H}_0/\hat{U}_0$ (where \hat{U}_0 is a characteristic flow speed), and a fluid density $\hat{\rho}_f$:

$$\begin{aligned} \mathbf{c}_i &= \hat{\mathbf{c}}_i/\hat{c}, & \mathbf{x} &= \hat{\mathbf{x}}/\hat{H}_0, \\ t &= \hat{t}/\hat{t}_0, \\ \Delta\mathbf{x} &= \Delta\hat{\mathbf{x}}/\hat{H}_0, & \Delta t &= \Delta\hat{t}/\hat{t}_0, \\ f_i &= \hat{f}_i/\hat{\rho}_f, & \mathbf{u} &= \hat{\mathbf{u}}/\hat{c}, \\ p &= \hat{p}/(\hat{\rho}_f\hat{c}^2), & \sigma_{\alpha\beta} &= \hat{\sigma}_{\alpha\beta}/(\hat{\rho}_f\hat{c}^2), \\ \nu &= \hat{\nu}/(\hat{c}\hat{H}_0), & \mathbf{g} &= \hat{\mathbf{g}}\hat{H}_0/(\hat{\rho}_f\hat{c}^2), \\ \mathbf{X}_k &= \hat{\mathbf{X}}_k/\hat{H}_0, & \mathbf{U}_k &= \hat{\mathbf{U}}_k/\hat{c}, \\ \mathbf{P} &= \hat{\mathbf{P}}/(\hat{\rho}_f\hat{c}^2), & \mathbf{X}_c &= \hat{\mathbf{X}}_c/\hat{H}_0, \\ \mathbf{F} &= \hat{\mathbf{F}}/(\hat{\rho}_f\hat{c}^2\hat{H}_0^2), & \mathbf{T} &= \hat{\mathbf{T}}/(\hat{\rho}_f\hat{c}^2\hat{H}_0^3), \end{aligned}$$

where the hat indicates a dimensional variable. It should be noted that the time step $\Delta\hat{t}$ is equal to the time span during which the particles travel one lattice spacing, i.e., $\Delta\hat{\mathbf{x}}/\Delta\hat{t} = \hat{c}$. From this relation, we can easily obtain $\Delta t = Sh \Delta x$ [where $Sh = \hat{H}_0/(\hat{t}_0\hat{c}) = \hat{U}_0/\hat{c}$].

APPENDIX B: DEPENDENCE OF THE RELAXATION RANGE α_b

In this section, we check the dependence of the relaxation range α_b , which is introduced to relax the bounce-back condition in Sec. II A. We simulate the flow over a stationary circular cylinder at $Re = 40$ (see Sec. III A) for various values of α_b .

Figure 16 shows the pressure coefficient C_p and the skin-friction coefficient C_f on the circular cylinder. We can see from Fig. 16(a) that the results for $\alpha_b = 0^\circ$ and 10° include the spurious oscillation in the distribution of C_p , whereas the results for $\alpha \geq 22.5^\circ$ do not include and almost overlap with each other. This result suggests that when α_b is too small, at most about 10° , the spurious oscillation of the local force cannot be suppressed. On the other hand, even when α_b is too large, there seems to be no problem in the distribution of C_p . This is because the preprocessing introduced in Sec. II B effectively prevents the PDFs in the normal direction from passing through the boundary despite the relaxation of the bounce-back condition.

However, from Fig. 16(b), we can see that for $\alpha_b \geq 30^\circ$ the skin-friction coefficient C_f is clearly underestimated. This is because when α_b is too large, at least about 30° , the PDFs in the tangential direction pass through the boundary, and the flow can slip along the boundary.

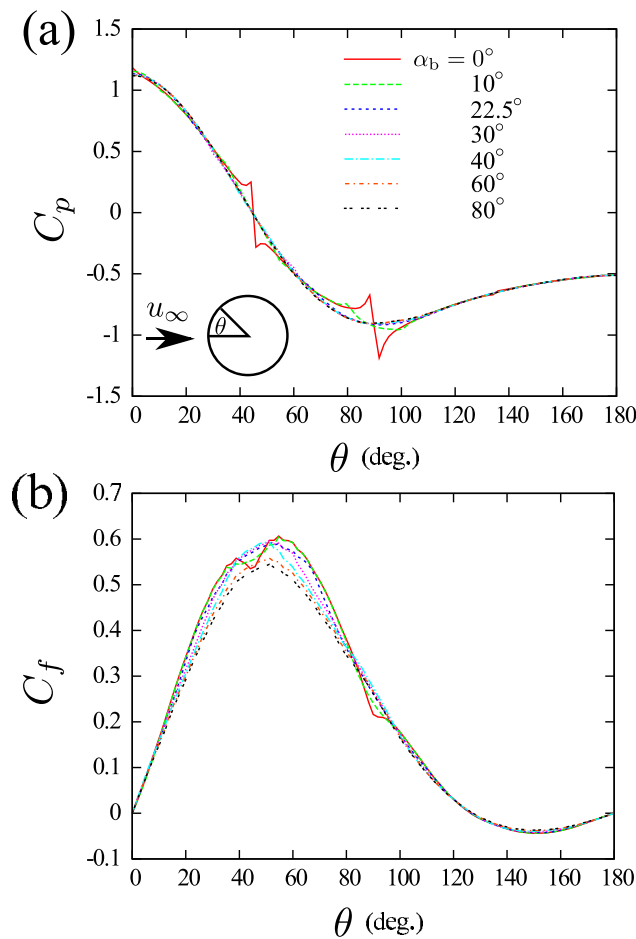


FIG. 16. Distributions of (a) the pressure coefficient C_p and (b) the skin-friction coefficient C_f on the circular cylinder in a uniform flow at $Re = 40$ for various values of the relaxation range α_b .

These results suggest that the value of α_b should be set in the range $10^\circ < \alpha_b < 30^\circ$. In the present study, therefore, we set $\alpha_b = 22.5^\circ$, which is equal to the half of the angle between adjacent particle velocities in the D2Q9 model (e.g., c_2 and c_6).

DATA AVAILABILITY

The data that support the findings of this study are available from the corresponding author upon reasonable request.

REFERENCES

- C. S. Peskin, "Flow patterns around heart valves: A numerical method," *J. Comput. Phys.* **10**, 252–271 (1972).
- C. S. Peskin, "Numerical analysis of blood flow in the heart," *J. Comput. Phys.* **25**, 220–252 (1977).
- R. Mittal and G. Iaccarino, "Immersed boundary methods," *Annu. Rev. Fluid Mech.* **37**, 239–261 (2005).
- J. Mohd-Yusof, "Combined immersed-boundary/B-spline methods for simulations of flow in complex geometries," in *CTR Annual Research Briefs* (NASA Ames/Stanford University, 1997), pp. 317–327.
- S. Kang and Y. Hassan, "A comparative study of direct-forcing immersed boundary–lattice Boltzmann methods for stationary complex boundaries," *Int. J. Numer. Methods Fluids* **66**, 1132–1158 (2011).
- E. A. Fadlun, R. Verzicco, P. Orlandi, and J. Mohd-Yusof, "Combined immersed-boundary finite-difference methods for three-dimensional complex flow simulations," *J. Comput. Phys.* **161**, 35–60 (2000).
- J. H. Seo and R. Mittal, "A sharp-interface immersed boundary method with improved mass conservation and reduced spurious pressure oscillations," *J. Comput. Phys.* **230**, 7347–7363 (2011).
- C. S. Peskin, "The immersed boundary method," *Acta Numer.* **11**, 479–517 (2002).
- M. Uhlmann, "An immersed boundary method with direct forcing for the simulation of particulate flows," *J. Comput. Phys.* **209**, 448–476 (2005).
- Z. G. Feng and E. E. Michaelides, "Robust treatment of no-slip boundary condition and velocity updating for the lattice-Boltzmann simulation of particulate flows," *Comput. Fluids* **38**, 370–381 (2009).
- T. Krüger, F. Varnik, and D. Raabe, "Efficient and accurate simulations of deformable particles immersed in a fluid using a combined immersed boundary lattice Boltzmann finite element method," *Comput. Math. Appl.* **61**, 3485–3505 (2011).
- M. Vanella and E. Balaras, "A moving-least-squares reconstruction for embedded-boundary formulations," *J. Comput. Phys.* **228**, 6617–6628 (2009).
- A. Posa, M. Vanella, and E. Balaras, "An adaptive reconstruction for Lagrangian, direct-forcing, immersed-boundary methods," *J. Comput. Phys.* **351**, 422–436 (2017).
- K. Suzuki and M. Yoshino, "A stress tensor discontinuity-based immersed boundary–lattice Boltzmann method," *Comput. Fluids* **172**, 593–608 (2018).
- S. Chen and G. D. Doolen, "Lattice Boltzmann method for fluid flows," *Annu. Rev. Fluid Mech.* **30**, 329–364 (1998).
- S. Succi, *The Lattice Boltzmann Equation for Fluid Dynamics and Beyond* (Oxford University Press, Oxford, 2001).
- R. Mei, D. Yu, and W. Shyy, "Force evaluation in the lattice Boltzmann method involving curved geometry," *Phys. Rev. E* **65**, 041203 (2002).
- D. Yu, R. Mei, L. S. Luo, and W. Shyy, "Viscous flow computations with the method of lattice Boltzmann equation," *Prog. Aerosp. Sci.* **39**, 329–367 (2003).
- P. Lallemand and L. S. Luo, "Lattice Boltzmann method for moving boundaries," *J. Comput. Phys.* **184**, 406–421 (2003).
- Z. G. Feng and E. E. Michaelides, "Proteus: A direct forcing method in the simulations of particulate flows," *J. Comput. Phys.* **202**, 20–51 (2005).
- X. D. Niu, C. Shu, Y. T. Chew, and Y. Peng, "A momentum exchange-based immersed boundary–lattice Boltzmann method for simulating incompressible viscous flows," *Phys. Lett. A* **354**, 173–182 (2006).
- J. Wu and C. Shu, "Implicit velocity correction-based immersed boundary–lattice Boltzmann method and its applications," *J. Comput. Phys.* **228**, 1963–1979 (2009).
- K. Suzuki and T. Inamuro, "Effect of internal mass in the simulation of a moving body by the immersed boundary method," *Comput. Fluids* **49**, 173–187 (2011).
- M. Jiang and Z. Liu, "A boundary thickening-based direct forcing immersed boundary method for fully resolved simulation of particle-laden flows," *J. Comput. Phys.* **390**, 203–231 (2019).
- S. Tao, W. He, J. Chen, B. Chen, G. Yang, and Z. Wu, "A non-iterative immersed boundary–lattice Boltzmann method with boundary condition enforced for fluid–solid flows," *Appl. Math. Modell.* **76**, 362–379 (2019).
- Z. Wang, Y. Wei, and Y. Qian, "A bounce back-immersed boundary–lattice Boltzmann model for curved boundary," *Appl. Math. Model.* **81**, 428–440 (2020).
- A. Goza, S. Liska, B. Morley, and T. Collonius, "Accurate computation of surface stresses and forces with immersed boundary methods," *J. Comput. Phys.* **321**, 860–873 (2016).
- X. He and L.-S. Luo, "Lattice Boltzmann model for the incompressible Navier–Stokes equation," *J. Stat. Phys.* **88**, 927–944 (1997).
- T. Inamuro, M. Yoshino, and F. Ogino, "Accuracy of the lattice Boltzmann method for small Knudsen number with finite Reynolds number," *Phys. Fluid* **9**, 3535–3542 (1997).
- Y. Nakayama and R. Yamamoto, "Simulation method to resolve hydrodynamic interactions in colloidal dispersions," *Phys. Rev. E* **71**, 036707 (2005).

- ³¹S. Jafari, R. Yamamoto, and M. Rahnama, "Lattice-Boltzmann method combined with smoothed-profile method for particulate suspensions," *Phys. Rev. E* **83**, 026702 (2011).
- ³²Y. Mino, H. Shinto, S. Sakai, and H. Matsuyama, "Effect of internal mass in the lattice Boltzmann simulation of moving solid bodies by the smoothed-profile method," *Phys. Rev. E* **95**, 043309 (2017).
- ³³X. He and G. Doolen, "Lattice Boltzmann method on curvilinear coordinates system: Flow around a circular cylinder," *J. Comput. Phys.* **134**, 306–315 (1997).
- ³⁴J. Park, K. Kwon, and H. Choi, "Numerical solutions of flow past a circular cylinder at Reynolds number up to 160," *KSME Int. J.* **12**, 1200–1205 (1998).
- ³⁵Y. Tseng and J. H. Ferziger, "A ghost-cell immersed boundary method for flow in complex geometry," *J. Comput. Phys.* **192**, 593–623 (2003).
- ³⁶D. J. Tritton, "Experiments on the flow past a circular cylinder at low Reynolds number," *J. Fluid Mech.* **6**, 547–567 (1959).
- ³⁷M. Coutanceau and R. Bouard, "Experimental determination of the main features of the viscous flow in the wake of a circular cylinder in uniform translation," *J. Fluid Mech.* **79**, 231–256 (1977).
- ³⁸S. C. R. Dennis and G. Cheng, "Numerical solutions for steady flow past a circular cylinder at Reynolds number up to 100," *J. Fluid Mech.* **42**, 471–489 (1970).
- ³⁹K. Taira and T. Colonius, "The immersed boundary method: A projection approach," *J. Comput. Phys.* **225**, 2118–2137 (2007).
- ⁴⁰B. N. Rajani, A. Kandasamy, and S. Majumdar, "Numerical simulation of laminar flow past a circular cylinder," *Appl. Math. Modell.* **33**, 1228–1247 (2009).
- ⁴¹A. Roshko, "On the development of turbulent wakes from vortex streets," NACA Report No. 1191 (National Advisory Committee for Aeronautics, Washington, DC, 1954).
- ⁴²C. Liu, X. Zheng, and C. H. Sung, "Preconditioned multigrid methods for unsteady incompressible flows," *J. Comput. Phys.* **139**, 35–57 (1998).
- ⁴³M. N. Linnick and H. F. Fasel, "A high-order immersed interface method for simulating unsteady incompressible flows on irregular domains," *J. Comput. Phys.* **204**, 157–192 (2005).
- ⁴⁴Y. Wang, C. Shu, C. J. Teo, and J. Wu, "An immersed boundary–lattice Boltzmann flux solver and its applications to fluid–structure interaction problems," *J. Fluid Struct.* **54**, 440–465 (2015).
- ⁴⁵H. Dütsch, F. Durst, S. Becker, and H. Lienhart, "Low-Reynolds-number flow around an oscillating circular cylinder at low Keulegan–Carpenter numbers," *J. Fluid Mech.* **360**, 249–271 (1998).
- ⁴⁶J. Feng, H. H. Hu, and D. D. Joseph, "Direct simulation of initial value problems for the motion of solid bodies in a Newtonian fluid. Part 2. Couette and Poiseuille flows," *J. Fluid Mech.* **277**, 271–301 (1994).
- ⁴⁷A. ten Cate, C. H. Nieuwstadt, J. J. Derksen, and H. E. A. Van den Akker, "Particle imaging velocimetry experiments and lattice-Boltzmann simulations on a single sphere settling under gravity," *Phys. Fluids* **14**, 4012–4025 (2002).
- ⁴⁸F. X. Giraldo, "Lagrange–Galerkin methods on spherical geodesic grid," *J. Comput. Phys.* **136**, 197–213 (1997).
- ⁴⁹S. P. Sane, "The aerodynamics of insect flight," *J. Exp. Biol.* **206**, 4191–4208 (2003).
- ⁵⁰M. Sun and J. Tang, "Unsteady aerodynamic force generation by a model fruit fly wing in flapping motion," *J. Exp. Biol.* **205**, 55–70 (2002), available at <https://jeb.biologists.org/content/205/1/55>.
- ⁵¹R. B. Srygley and A. L. R. Thomas, "Unconventional lift-generating mechanisms in free-flying butterflies," *Nature* **420**, 660–664 (2002).
- ⁵²K. Suzuki, T. Kato, K. Tsue, M. Yoshino, and M. Denda, "Comparative study between a discrete vortex method and an immersed boundary–lattice Boltzmann method in 2D flapping flight analysis," *Int. J. Mod. Phys. C* **32**, 2150005 (2021).
- ⁵³N. Yokoyama, K. Senda, M. Iima, and N. Hirai, "Aerodynamic forces and vortical structures in flapping butterfly's forward flight," *Phys. Fluids* **25**, 021902 (2013).
- ⁵⁴K. Suzuki, K. Minami, and T. Inamuro, "Lift and thrust generation by a butterfly-like flapping wing–body model: Immersed boundary–lattice Boltzmann simulations," *J. Fluid Mech.* **767**, 659–695 (2015).
- ⁵⁵M. Fuchiwaki and K. Tanaka, "Three-dimensional vortex structure in a wake of a free-flight butterfly," *Trans. JSME* **82**, 15 (2016).
- ⁵⁶Y.-H. J. Fei and J.-T. Yang, "Importance of body rotation during the flight of a butterfly," *Phys. Rev. E* **93**, 033124 (2016).
- ⁵⁷C. Körner, M. Thies, T. Hofmann, N. Thürey, and U. Rüde, "Lattice Boltzmann model for free surface flow for modeling foaming," *J. Stat. Phys.* **121**, 179–196 (2005).